Open Research Online

The Open University's repository of research publications
and other research outputs

Linking ice and gas in the σ Orionis Barnard 35A cloud

Journal Item

oro.open.ac.uk

Astronomy & Astrophysics

Linking ice and gas in the λ Orionis Barnard 35A cloud

G. Perotti[1] , J. K. Jørgensen[1] , H. J. Fraser[2] , A. N. Suutarinen[2] , L. E. Kristensen[1] , W. R. M. Rocha[1] ,
P. Bjerkeli[3] , and K. M. Pontoppidan[4]

[1] Niels Bohr Institute & Centre for Star and Planet Formation, University of Copenhagen, Øster Voldgade 5−7, 1350 Copenhagen K.,
Denmark
e-mail: giulia.perotti@nbi.ku.dk
[2] School of Physical Sciences, The Open University, Walton Hall, Milton Keynes, MK7 6AA, UK
[3] Department of Space, Earth, and Environment, Chalmers University of Technology, Onsala Space Observatory, 439 92 Onsala,
Sweden
[4] Space Telescope Science Institute, 3700 San Martin Drive, Baltimore, MD 21218, USA

ABSTRACT

Context. Dust grains play an important role in the synthesis of molecules in the interstellar medium, from the simplest species, such as H_2, to complex organic molecules. How some of these solid-state molecules are converted into gas-phase species is still a matter of debate.
Aims. Our aim is to directly compare ice and gas abundances of methanol (CH_3OH) and carbon monoxide (CO) obtained from near-infrared (2.5−5 μm) and millimetre (1.3 mm) observations and to investigate the relationship between ice, dust, and gas in low-mass protostellar envelopes.
Methods. We present Submillimeter Array (SMA) and Atacama Pathfinder EXperiment (APEX) observations of gas-phase CH_3OH ($J_K = 5_K − 4_K$), ^{13}CO, and $C^{18}O$ ($J = 2 − 1$) towards the multiple protostellar system IRAS 05417+0907, which is located in the B35A cloud, λ Orionis region. We use archival IRAM 30 m data and AKARI H_2O, CO, and CH_3OH ice observations towards the same target to compare ice and gas abundances and directly calculate CH_3OH and CO gas-to-ice ratios.
Results. The CO isotopologue emissions are extended, whereas the CH_3OH emission is compact and traces the giant molecular outflow emanating from IRAS 05417+0907. A discrepancy between sub-millimetre dust emission and H_2O ice column density is found for B35A−4 and B35A−5, similar to what has previously been reported. B35A−2 and B35A−3 are located where the sub-millimetre dust emission peaks and show H_2O column densities lower than that of B35A−4.
Conclusions. The difference between the sub-millimetre continuum emission and the infrared H_2O ice observations suggests that the distributions of dust and H_2O ice differ around the young stellar objects in this dense cloud. The reason for this may be that the four sources are located in different environments resolved by the interferometric observations: B35A−2, B35A−3, and, in particular, B35A−5 are situated in a shocked region that is plausibly affected by sputtering and heating, which in turn impacts the sub-millimetre dust emission pattern, while B35A−4 is situated in a more quiescent part of the cloud. Gas and ice maps are essential for connecting small-scale variations in the ice composition with the large-scale astrophysical phenomena probed by gas observations.

Key words. ISM: molecules – stars: protostars – astrochemistry – molecular processes – ISM: individual objects: Orion

1. Introduction

The interaction between dust, ice, and gas is ubiquitous in star-forming regions, and it is essential for the synthesis of interstellar molecules, the main ingredients for the origin of life on Earth. In recent decades, the number of detected molecules in the interstellar medium (ISM) increased considerably (McGuire 2018) and with it the awareness of an interplay between solid and gaseous molecules in star-forming regions (Herbst & van Dishoeck 2009; Boogert et al. 2015; Jørgensen et al. 2020; Öberg & Bergin 2021). Some of the questions that remain to be answered regard the link between the distribution of solids (dust, ices) and gaseous molecules in molecular clouds and what this tells us about the solid-gas intertwined chemistries (e.g. the thermal and non-thermal desorption mechanisms that release solid-state molecules into the gas phase and vice versa).

Desorption mechanisms are of the utmost importance for understanding some critical aspects of star and planet formation (van Dishoeck & Blake 1998). Besides enhancing the chemical complexity in the gas phase (Cazaux et al. 2003; Jørgensen et al. 2016; Bergner et al. 2017; Calcutt et al. 2018; Manigand et al. 2020; van Gelder et al. 2020), the positions in protostellar disks at which they occur (i.e. snow lines) influence the formation and evolution of planets (Öberg et al. 2011; Eistrup et al. 2016; van 't Hoff et al. 2017; Grassi et al. 2020). Simultaneously, desorption processes can also shape the composition of grain surfaces. This is a consequence of the fact that all desorption mechanisms are much more efficient for volatile species (CO, O_2, and N_2; Bisschop et al. 2006; Noble et al. 2012; Cazaux et al. 2017) than for less volatile species (H_2O and CH_3OH; Fraser et al. 2001; Bertin et al. 2016; Cruz-Diaz et al. 2016; Martín-Doménech et al. 2016). Since thermal desorption mechanisms alone can often not account for the diversity of species observed in star-forming regions, a further question remains as to the extent that the prevailing physical conditions might impact ice loss, for example through photo-desorption, sputtering, and chemical- and shock-induced processes (e.g. Kristensen et al. 2010; Vasyunin & Herbst 2013; Dulieu et al. 2013; Öberg 2016; Dartois et al. 2019). Obtaining key insights into the desorption mechanisms is crucial for studying the composition of ice
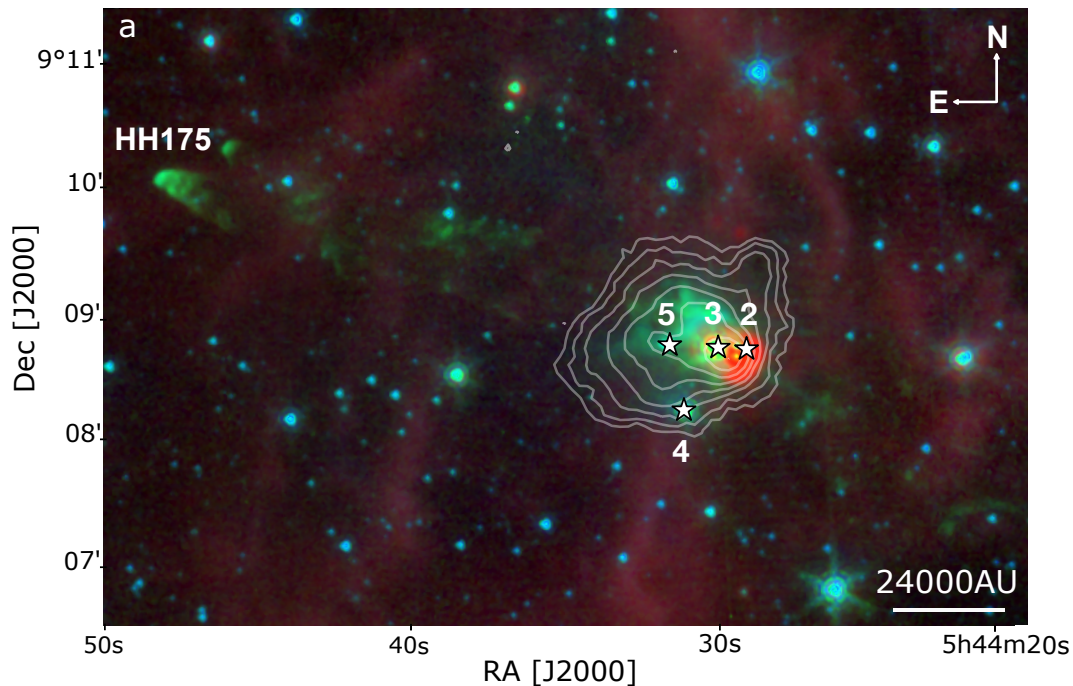
Fig. 1. Three-colour image of B35A overlaid with SCUBA−2 850 μm density flux in units of mJy beam^{-1} (Reipurth & Friberg 2021); contours are in decreasing steps of 30% starting at 7.3 Jy beam^{-1}. The composite is made from *Spitzer* IRAC 3.6 μm (blue), 4.5 μm (green), and Multiband Imaging Photometer for *Spitzer* (MIPS) 24.0 μm (red) bands (programme ID: 139, PI: N. J. Evans II). The white stars mark the positions of the AKARI and *Spitzer* c2d identified B35A sources. Connelley et al. (2008) and Reipurth & Friberg (2021) show the B35A sources to be multiplet systems totalling four or five objects.

mantles, and hence the production of complex organics, during the early phases of star formation.

The preferred observational approach for constraining solid-state chemistry consists of inferring abundances of solid-state molecules based on their observed gas-phase emissions (Bergin & Tafalla 2007; Öberg et al. 2009; Whittet et al. 2011). Although this method of indirectly deriving ice abundances from gas-phase observations is the most used to get insights into the ice composition, it relies on major assumptions, for instance on the formation pathways and the desorption efficiency of solid-state species.

One way to test these assumptions is to combine ice and gas observations (i.e. ice- and gas-mapping techniques) and thus compare ice abundances with gas abundances towards the same region (Noble et al. 2017; Perotti et al. 2020). The evident advantage of combining the two techniques is that it enables us to study the distribution of gas-phase and solid-state molecules concurrently on the same lines of sight, and hence to address how solid-state processes are affected by physical conditions probed by gas-phase mapping, such as density, temperature and radiation field gradients, turbulence, and dust heating. However, the number of regions where such combined maps are available is still limited.

In this article we explore the interplay between ice and gas in the bright-rimmed cloud Barnard 35 (B35A; also known as BRC18, SFO18, and L1594), which is located in the λ Orionis star-forming region (Sharpless 1959; Lada & Black 1976; Murdin & Penston 1977; Mathieu 2008; Hernández et al. 2009; Bayo et al. 2011; Barrado et al. 2011; Kounkel et al. 2018; Ansdell et al. 2020) at a distance of 410 ± 20 pc (*Gaia* DR2; Zucker et al. 2019, 2020). The λ Orionis region is characterised by a core of OB stars enclosed in a ring of dust and gas (Wade 1957; Heiles & Habing 1974; Maddalena & Morris 1987;

Zhang et al. 1989; Lang et al. 2000; Dolan & Mathieu 2002; Sahan & Haffner 2016). The OB stars formed approximately 5 Myr ago, whereas the timing of the ring formation is less certain; it occurred between 1 and 6 Myr ago as the consequence of a supernova explosion (Dolan & Mathieu 1999, 2002; Kounkel 2020). The presence of strong stellar winds from the massive stars and ionisation fronts in the region has shaped and ionised the neighbouring ring of gas, leading to the formation of dense molecular clouds (e.g. B35A and B30; Barrado et al. 2018) and photodissociation regions (PDRs; Wolfire et al. 1989; De Vries et al. 2002; Lee et al. 2005). For instance, the stellar wind from λ Orionis, the most massive star of the Collinder 69 cluster (an O8III star; Conti & Leep 1974), hits the western side of B35A, compressing the cloud and forming a PDR between the molecular cloud edge and the extended HII region S264 (De Vries et al. 2002; Craigon 2015).

Star formation is currently occurring in B35A: the multiple protostellar system IRAS 05417+0907 (i.e. B35A−3) lies within the western side of the cloud (Fig. 1). IRAS 05417+0907 was long thought to be a single source, but it is in fact a cluster of at least four objects (B35A−2, B35A−3, B35A−4, and B35A−5), which were partially resolved by *Spitzer* InfraRed Array Camera (IRAC) observations as part of the *Spitzer* Legacy Program "From Molecular Cores to Planet-forming Disks[1]" ("c2d"; Evans et al. 2014; Table 1). B35A−3 (i.e. IRAS 05417+0907) is a Class I young stellar object (YSO), and it is the primary of a close binary system (Connelley et al. 2008); the classification of the other sources remains uncertain. B35A−3 emanates a giant bipolar molecular outflow extending in the NE-SW direction relative to λ Orionis and terminating at the Herbig-Haro object

---

[1] https://irsa.ipac.caltech.edu/data/SPITZER/C2D/cores.html

Table 1. Sample of sources.

Object[a]	RA [J2000]	Dec [J2000]	A_V [mag]
B35A−2	05:44:29.30	+09:08:57.0	52.7[b]
B35A−3	05:44:30.00	+09:08:57.3	54.9 ± 0.2[c]
B35A−4	05:44:30.85	+09:08:26.0	49.6 ± 2.3[c]
B35A−5	05:44:31.64	+09:08:57.8	19.5 ± 1.5[c]

Notes. [a]The objects are numbered according to the ID used in Noble et al. (2013). In Noble et al. (2017), objects 2, 3, 4, and 5 are numbered 11, 1, 6, and 12, respectively. [b]For a detailed description of the A_V determination for B35A−2, see Sect. 3.3 and Appendix B. [c]From the *Spitzer* c2d catalogue (https://irsa.ipac.caltech.edu/data/SPITZER/C2D/cores.html).

HH 175 (Myers et al. 1988; Qin & Wu 2003; Craigon 2015; Reipurth 2000). A detailed multi-wavelength analysis and characterisation of HH 175 and of the multiple protostellar system is presented by Reipurth & Friberg (2021).

The ice reservoir towards the YSOs in B35A has been extensively studied by Noble et al. (2013, 2017) and Suutarinen (2015). These works were based on near-infrared (NIR) spectroscopic observations (2.5−5 μm) with the AKARI satellite. In Noble et al. (2013), H_2O, CO_2, and CO ice features were identified towards all four YSOs; Suutarinen (2015) performed a multi-component, multi-line fitting of all the ice features towards the same B35A sources identified by Noble et al. (2013) and Evans et al. (2014) and, in a method similar to that employed by Perotti et al. (2020), were able to concurrently extract the H_2O, CO, and CH_3OH ice column densities from the spectral data. These are the ice column densities used for comparison in the remainder of this paper.

In parallel, the morphology and kinematics of the gas in B35A have been investigated using single dishes, such as the *James Clerk Maxwell* Telescope (JCMT) and the Institut de Radio Astronomie Millimétrique (IRAM) 30 m telescope by Craigon (2015). The survey mapped ^{12}CO, ^{13}CO, and $C^{18}O$ $J = 3−2$ and $J = 2−1$ over a $14.6' \times 14.6'$ region and confirmed the existence of a bright and dense rim along the western side of B35A, which is heated and compressed by the stellar wind of the nearby λ Orionis, and of a giant bipolar outflow emanating from the YSO region.

To investigate the interaction between the solid (ice) and gas phases in the region, ice maps of B35A were compared to gas-phase maps in Noble et al. (2017). No clear correlation was found between gas or dust to ice towards B35A from this combination of ice- and gas-mapping techniques. The local scale variations traced by the ice mapping were not immediately related to large-scale astrophysical processes probed by the dust and gas observations.

In this paper, we present interferometric Submillimeter Array (SMA) observations of the $J_K = 5_K−4_K$ rotational band of CH_3OH at 241.791 GHz and of the $J = 2−1$ rotational bands of two CO isotopologues (^{13}CO and $C^{18}O$) towards the multiple protostellar system IRAS 05417+0907 in B35A. The angular resolution of the interferometric observations allows us to study the distribution of the targeted species in greater spatial detail compared to existing single-dish observations. To also recover the large-scale emission, the SMA observations are combined with single-dish data, thus resolving the protostellar system members and, concurrently, probing the surrounding cloud. Furthermore, we produce ice and gas maps of a pivotal complex molecule,

CH_3OH, and of one of its precursors, CO, to analyse the gas and ice interplay in the region. Lastly, we directly calculate the gas-to-ice ratios of B35A to compare them with ratios obtained for nearby star-forming regions.

The article is organised as follows. Section 2 describes the gas-phase observations and the archival data used to produce the gas and ice maps. Section 3 presents the results of the observations. Section 4 analyses the variations between the gas-phase and solid-state distributions of the different molecules. Section 5 discusses the observational results with a particular focus on the obtained gas-to-ice ratios. Finally, Sect. 6 summarises the main conclusions.

2. Observations and archival data

2.1. SMA and APEX observations

The sample of sources was observed on September 19, 2018, with the SMA (Ho et al. 2004). The array was in its subcompact configuration with seven operating antennas. The targeted region was covered by two overlapping pointings; the first pointing was centred on B35A−3 (i.e. IRAS 05417+0907), and the second was offset by one half primary beam to the south-east. Their exact coordinates are $\alpha_{J2000} = 05^h44^m30\overset{s}{.}00$, $\delta_{J2000} = +09°08'57\overset{''}{.}3$ and $\alpha_{J2000} = 05^h44^m30\overset{s}{.}58$, $\delta_{J2000} = +09°08'33\overset{''}{.}8$, respectively.

The SMA observations probed frequencies spanning from 214.3 to 245.6 GHz with a spectral resolution of 0.1 MHz (0.135 km s^{-1}). This frequency range covers, among other species, the CH_3OH $J_K = 5_K−4_K$ branch at 241.791 GHz, ^{13}CO $J = 2−1$ at 220.398 GHz, and $C^{18}O$ $J = 2−1$ at 219.560 GHz (Table 2). The observational setup consisted of a first long integration on the bandpass calibrator, the strong quasar 3c84, followed by alternated integrations on the source and on the gain calibrator, the quasar J0510+180. The absolute flux scale was obtained through observations of Uranus. The SMA dataset was both calibrated and imaged using the Common Astronomy Software Applications package[2] (CASA; McMullin et al. 2007). At these frequencies, the typical SMA beam sizes were $7\overset{''}{.}3 \times 2\overset{''}{.}4$ with a position angle of $-32.2°$ for CH_3OH and $7\overset{''}{.}9 \times 2\overset{''}{.}6$ with a position angle of $-31.2°$ for ^{13}CO and $C^{18}O$.

To trace the more extended structures in the region, the SMA data were complemented by maps obtained using the Atacama Pathfinder EXperiment (APEX; Güsten et al. 2006) on August 20−22, 2018. The single-dish observations covered frequencies between 236−243.8 GHz, matching the SMA 240 GHz receiver upper side band. The spectral resolution of the APEX observations was 0.061 MHz (0.076 km s^{-1}). The APEX map size was $100'' \times 125''$, and it extended over both SMA primary beams. The coordinates of the APEX pointing are $\alpha_{J2000} = 05^h44^m30\overset{s}{.}00$, $\delta_{J2000} = +09°08'57\overset{''}{.}3$. The APEX beam size was $27\overset{''}{.}4$ for the CH_3OH $J_K = 5_K−4_K$ lines emission. The APEX dataset was reduced using the GILDAS package CLASS[3]. At a later stage, the reduced APEX data cube was imported to CASA and combined with the interferometric data using the feathering technique. A description of the combination procedure is given in Appendix A.1.

2.2. JCMT/SCUBA-2, Spitzer IRAC, 2MASS, IRAM 30 m, and AKARI data

Ancillary data to the SMA and APEX observations were adopted in this study. To construct H_2 column density maps of B35A, we used sub-millimetre continuum maps at 850 μm obtained

---

[2] http://casa.nrao.edu/
[3] http://www.iram.fr/IRAMFR/GILDAS

Table 2. Spectral data of the detected molecular transitions.

Transition	Frequency[a] [GHz]	$A_{ul}^{(a)}$ [s^{-1}]	$g_u^{(a)}$	$E_u^{(a)}$ [K]	$n_{cr}^{(b)}$ [cm^{-3}]
C^{18}O $J = 2-1$	219.560	6.01×10^{-7}	5	15.9	9.3×10^3
^{13}CO $J = 2-1$	220.398	6.04×10^{-7}	5	15.9	9.4×10^3
CH$_3$OH $J = 5_0-4_0$ E$^+$	241.700	6.04×10^{-5}	11	47.9	5.5×10^5
CH$_3$OH $J = 5_1-4_1$ E$^-$	241.767	5.81×10^{-5}	11	40.4	4.8×10^5
CH$_3$OH $J = 5_0-4_0$ A$^+$	241.791	6.05×10^{-5}	11	34.8	5.0×10^5
CH$_3$OH $J = 5_1-4_1$ E$^+$	241.879	5.96×10^{-5}	11	55.9	4.9×10^5
CH$_3$OH $J = 5_2-4_2$ E$^-$	241.904	5.09×10^{-5}	11	60.7	4.2×10^5

Notes. [a]From the Cologne Database for Molecular Spectroscopy (CDMS; Müller et al. 2001) and the Jet Propulsion Laboratory catalogue (Pickett et al. 1998). [b]Calculated using a collisional temperature of 20 K and collisional rates from the Leiden Atomic and Molecular Database (LAMDA; Schöier et al. 2005). The references for the collisional rates are Yang et al. (2010) for the CO isotopologues and Rabli & Flower (2010) for CH$_3$OH.
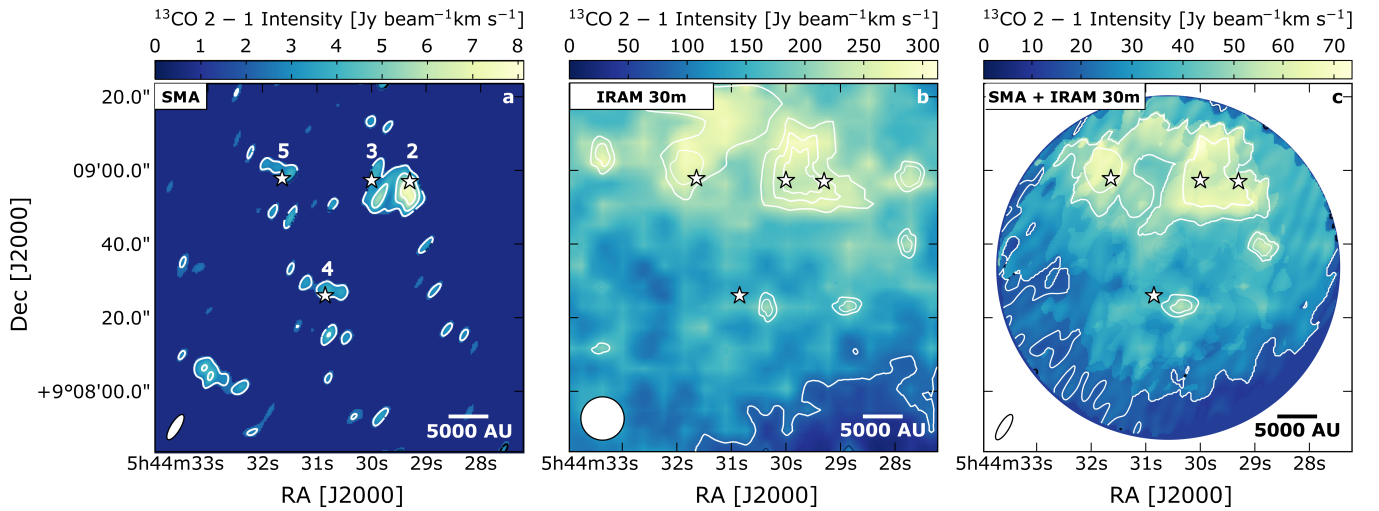
Fig. 2. Integrated intensity maps for ^{13}CO $J = 2-1$ detected by the SMA (*panel a*), by the IRAM 30 m telescope (*panel b*), and in the combined interferometric SMA and single-dish IRAM 30 m data (*panel c*). All lines are integrated between 7 and 16 km s^{-1}. Contours are at 5σ, 10σ, 15σ, etc. (σ_{SMA} = 0.42 Jy beam^{-1} km s^{-1}, $\sigma_{\text{IRAM 30 m}}$ = 6 Jy beam^{-1} km s^{-1}, $\sigma_{\text{SMA+IRAM 30 m}}$ = 1.03 Jy beam^{-1} km s^{-1}). *Panel c*: white area outlines the primary beam of the SMA observations. The synthesised beams are displayed in white in the bottom left corner of each panel. The white stars mark the positions of the targeted B35A sources.

with the SCUBA−2 camera at the JCMT by Reipurth & Friberg (2021), visual extinction values from the *Spitzer* c2d catalogue[4], and 2MASS and *Spitzer* IRAC photometric data (Skrutskie et al. 2006; Evans et al. 2014). IRAM 30 m telescope observations (Craigon 2015) were used to trace the extended emission for ^{13}CO and C^{18}O $J = 2-1$. Finally, to produce gas-ice maps of B35A, we made use of the ice column densities determined by Suutarinen (2015) from AKARI satellite observations.

3. Results

This section lists the observational results, supplying a summary of the methods employed to determine CO and CH$_3$OH gas column densities (Sect. 3.1 and Appendix A). Additionally, it presents the H$_2$O, CO, and CH$_3$OH ice column densities (Sect. 3.2) and the two H$_2$ column density maps used in the calculation of the abundances of the ice and gas species (Sect. 3.3).

4 https://irsa.ipac.caltech.edu/data/SPITZER/C2D/cores.html

3.1. Gas-phase species

The spectral line data of the detected molecular transitions are listed in Table 2. Figures 2–4 display moment 0 maps of the ^{13}CO and C^{18}O $J = 2-1$ lines and the CH$_3$OH $J = 5_0-4_0$ A$^+$ line created using SMA, IRAM 30 m, and APEX data. Moment 0 maps of the CH$_3$OH $J = 5_0-4_0$ A$^+$ line are presented in this section as this transition is the brightest of the CH$_3$OH $J = 5_K-4_K$ branch at 241.791 GHz. The maps show that the SMA observations filter out spatially extended emission related to the B35A cloud. The SMA data only recover ≈10% of the extended emission detected in the single-dish data. Consequently, we need to combine the interferometric data with the single-dish maps in order not to severely underestimate the column densities.

Panels a of Figs. 2–3 show that the interferometric emission is predominantly compact and the peak intensity is seen, for both CO isotopologues, at the location of B35A−2. The emission observed in the IRAM 30 m datasets (panels b of Figs. 2–3) is extended and mostly concentrated around B35A−2, B35A−3, and B35A−5. In the combined SMA + IRAM 30 m maps (panels c of Fig. 2–3), the peak emission is also located
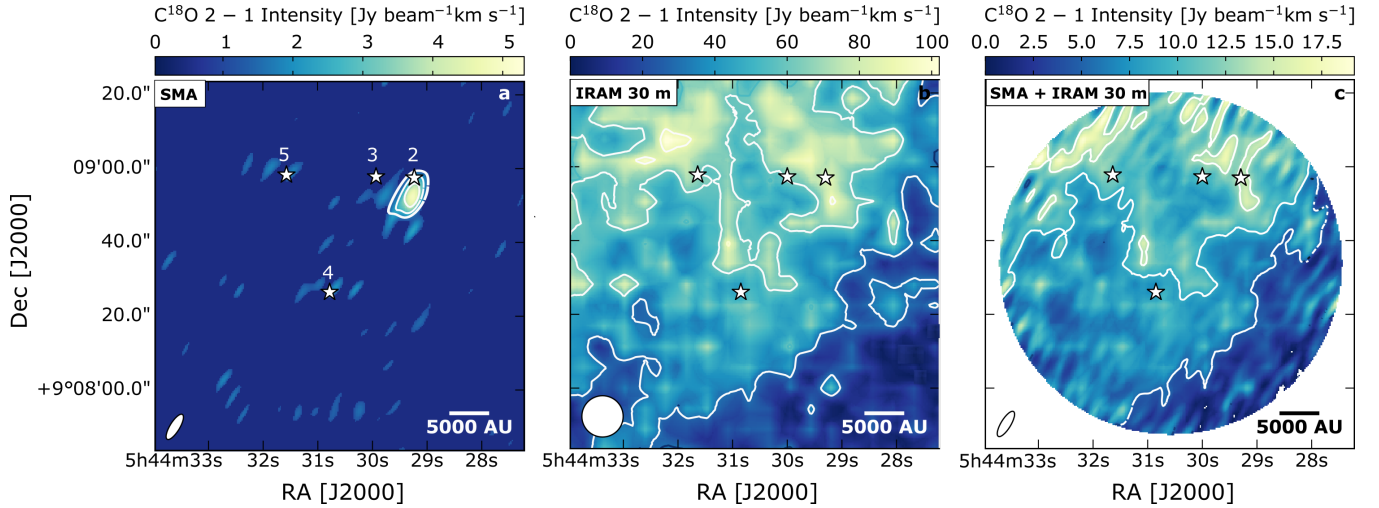
Fig. 3. Integrated intensity maps for $C^{18}O$ $J = 2$ detected by the SMA (*panel a*), by the IRAM 30 m telescope (*panel b*), and in the combined interferometric SMA and single-dish IRAM 30 m data (*panel c*). All lines are integrated between 10 and 15 km s^{-1}. Contours are at 5, 10, and 15σ (σ_{SMA} = 0.37 Jy beam^{-1} km s^{-1}, $\sigma_{IRAM\ 30\ m}$ = 5 Jy beam^{-1} km s^{-1}, $\sigma_{SMA+IRAM\ 30\ m}$ = 0.40 Jy beam^{-1} km s^{-1}). *Panel c*: white area outlines the primary beam of the SMA observations. The synthesised beams are displayed in white in the bottom left corner of each panel. The white stars mark the positions of the targeted B35A sources.
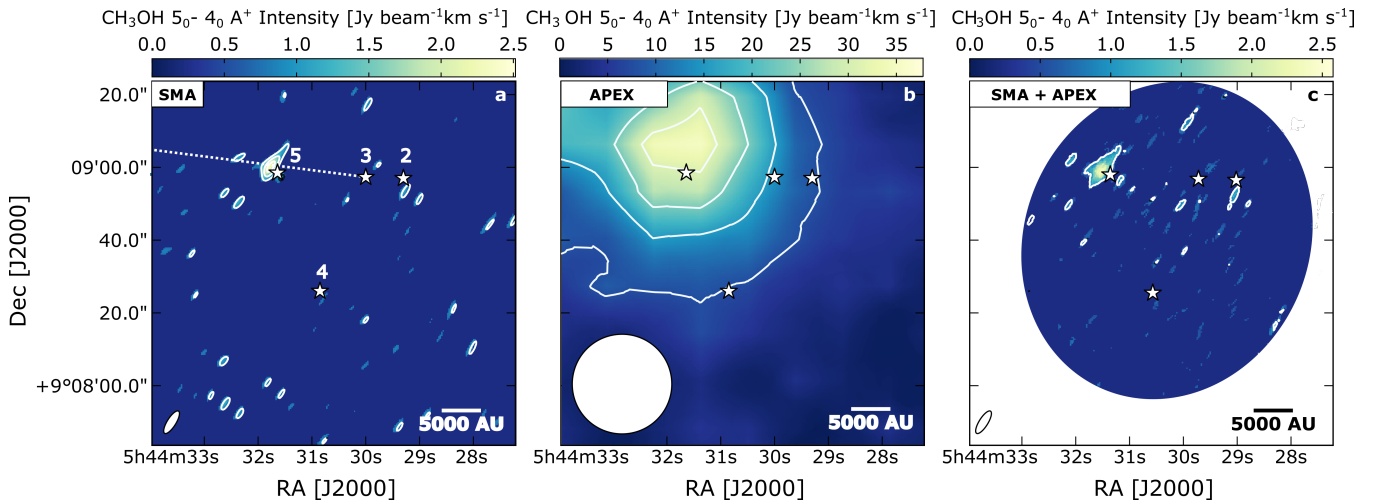
Fig. 4. Integrated intensity maps for CH_3OH $J = 5_0-4_0$ A$^+$ detected by the SMA (*panel a*), by the APEX telescope (*panel b*), and in the combined interferometric SMA and single-dish APEX data (*panel c*). All lines are integrated between 6 and 12.5 km s^{-1}. Contours start at 5σ (σ_{SMA} = 0.04 Jy beam^{-1} km s^{-1}, σ_{APEX} = 4 Jy beam^{-1} km s^{-1}, $\sigma_{SMA+APEX}$ = 0.04 Jy beam^{-1} km s^{-1}) and follow in steps of 5σ. *Panel c*: white area outlines the primary beam of the SMA observations. The synthesised beams are displayed in white in the bottom left corner of each panel. The white stars mark the positions of the targeted B35A sources, and the dotted blue line indicates the direction of the giant outflow terminating at HH 175.

in the region where B35A−2, B35A−3, and B35A−5 are present.

In contrast, the observed CH_3OH peak intensity is exclusively localised at the B35A−5 position in the SMA data (panel a of Fig. 4). B35A−5 lies along the eastern lobe of the giant bipolar molecular outflow emanated from IRAS 05417+0907 (i.e. B35A−3) and terminating at the location of the Herbig-Haro object HH 175 (Craigon 2015). The CH_3OH emission is extended in the APEX data (panel b of Fig. 4) and hence not resolved at one particular source position. The emission in the SMA + APEX moment 0 map (panel c of Fig. 4) is compact and concentrated in one ridge in the proximity of B35A−5. The channel maps (Figs. A.3−A.5) and the spectra (Fig. A.1) extracted from the combined interferometric and single-dish datasets show predominantly blue-shifted components (Appendix A.3). Blue- and red-shifted components are seen for the CO

isotopologues, which were previously observed by De Vries et al. (2002), Craigon (2015), and Reipurth & Friberg (2021) and attributed to outflowing gas.

The ^{13}CO emission is optically thick towards the B35A sources; therefore, the ^{13}CO column densities are underestimated towards the targeted region (Appendix A.2). Consequently, the optically thin $C^{18}O$ emission was adopted to estimate the column density of ^{12}CO in B35A. First, $C^{18}O$ column densities towards the protostellar system members were obtained from the integrated line intensities of the combined SMA + IRAM 30 m maps (panel c of Fig. 3), assuming optically thin emission and a kinetic temperature for the YSO region equal to 25 K (Craigon 2015). The formalism adopted in the column density calculation is presented in Appendix A.4, and the calculated $C^{18}O$ column densities and their uncertainties are listed in Table 3. The $C^{18}O$ column densities were converted to ^{12}CO column

Table 3. Total ice and gas column densities towards the B35A sources.

Object	$N^{ice}_{H_2O\ tot}$ $[10^{18}\ cm^{-2}]$	$N^{ice}_{CO\ tot}$ $[10^{18}\ cm^{-2}]$	$N^{ice}_{CH_3OH\ tot}$ $[10^{18}\ cm^{-2}]$	$N^{gas}_{C^{18}O\ tot}$ $[10^{15}\ cm^{-2}]$	$N^{gas}_{^{12}CO\ tot}$ $[10^{18}\ cm^{-2}]$	$N^{gas}_{CH_3OH\ tot}$ $[10^{14}\ cm^{-2}]$	$N^{SCUBA-2\ (\dagger)}_{H_2}$ $[10^{22}\ cm^{-2}]$	$N^{A_V}_{H_2}$ $[10^{22}\ cm^{-2}]$
B35A−2	2.96 ± 0.13	0.34 ± 0.03	0.26 ± 0.03	9.38 ± 1.92	5.22 ± 1.07	...	1.76 ± 0.09	$7.22^{(*)}$
B35A−3	2.96 ± 0.12	0.32 ± 0.03	0.16 ± 0.03	7.02 ± 1.44	3.91 ± 0.80	...	1.69 ± 0.08	7.52 ± 0.02
B35A−4	3.35 ± 0.11	0.28 ± 0.06	0.10 ± 0.06	4.99 ± 1.03	2.78 ± 0.57	...	0.39 ± 0.02	6.79 ± 0.68
B35A−5	0.78 ± 0.12	<0.18	<0.18	7.11 ± 1.46	3.96 ± 0.81	1.91 ± 0.24	1.09 ± 0.05	2.66 ± 0.20

Notes. Columns 2−4 display the ice column densities from Suutarinen (2015). Columns 5−7 list the gas column densities for $T_{rot} = 25$ K. The errors are estimated based on the rms noise of the spectra and on the ∼20% calibration uncertainty. Non-detections are indicated by ellipses. $^{(\dagger)}N^{SCUBA-2}_{H_2}$ is calculated using $T_{dust} = 25$ K. The errors are calculated from the 5% flux calibration uncertainty and do not take the uncertainty on the T_{dust} into account. $^{(*)}$The uncertainty on the A_V and consequently on the $N^{A_V}_{H_2}$ for B35−2 is not estimated because this object is not detected in the *J*, *H*, or *K* bands.

densities, assuming a $^{16}O/^{18}O$ isotope ratio of 557 ± 30 (Wilson 1999). The resulting ^{12}CO column densities (Table 3) are in good agreement with the values reported in Craigon (2015).

The CH_3OH column density towards B35A−5 was estimated from the integrated line intensities of the combined SMA + APEX maps for the five CH_3OH lines (Table A.2), assuming optically thin CH_3OH emission, a kinetic temperature of 25 K (Craigon 2015), and local thermodynamic equilibrium (LTE) conditions. The CH_3OH column density and its uncertainty are reported in Table 3. For all the gas-phase species, the uncertainty on the column densities was estimated based on the spectral rms noise and on the ∼20% calibration uncertainty.

3.2. Ice column densities

The ice column densities of H_2O, CO and CH_3OH used in this paper were originally derived by Suutarinen (2015) from the AKARI (2.5−5 μm) NIR spectra of the targeted B35A sources. Suutarinen (2015) adopted a non-heuristic approach, employing ice laboratory data and analytical functions to concurrently account for the contribution of a number of molecules to the observed ice band features. A detailed description of the AKARI observations is given in Noble et al. (2013), and the methodology adopted to derive the column densities of the major ice species can be found in Suutarinen (2015).

The total ice column densities from Suutarinen (2015) are listed in Table 3. Among the three molecules, H_2O ice is the most abundant in the ices of B35A, with column densities of up to $3.35 \times 10^{18}\ cm^{-2}$, followed by CO and CH_3OH (Table 3). The column densities of the latter two molecules are comparatively one order of magnitude less abundant than H_2O ice. Upper limits are given for the CO and CH_3OH column densities towards B35A−5 because of difficulties in distinguishing the absorption features in the spectrum of this YSO (Noble et al. 2013; Suutarinen 2015). A trend is observed for the CO and CH_3OH values: The column densities towards B35A−2 are the highest reported, followed by B35A−3, B35A−4, and B35A−5. The CO and CH_3OH ice column densities appear to follow the visual extinction, with B35A−2 and B35A−3 being the most extincted sources and showing the highest CO and CH_3OH column densities (Tables 1 and 3). In this regard, it is important to recall that B35A−2 is not detected in the *J*, *H*, or *K* bands, making the determination of its visual extinction uncertain (Sect. 3.3 and Appendix B).

3.3. H_2 column densities

An important factor to consider when combining ice- and gas-mapping techniques is that ice absorption and dust and gas emissions may probe different spatial scales (Noble et al. 2017). As a matter of fact, the targeted sources may be embedded to different depths in the B35A cloud, and, consequently, the gas and ice observations may not be tracing the same columns of material. Therefore, the search for gas-ice correlations towards B35A has to be performed by comparing gas and ice abundances relative to H_2, following the approach adopted in Perotti et al. (2020).

To keep the gas and ice observations in their own reference frame, two H_2 column density maps were produced: one to derive gas abundances and one to determine ice abundances (Fig. 5). For the gas observations, estimates of the H_2 column density were made using sub-millimetre continuum maps of B35A at 850 μm (SCUBA−2; Reipurth & Friberg 2021), under the assumption that the continuum emission originated from optically thin thermal dust radiation (Kauffmann et al. 2008). In this regime, the strength of the sub-millimetre radiation is dependent on the column density (N), the opacity (κ_ν), and the dust temperature (T). The adopted value for the opacity per unit dust+gas mass at 850 μm was 0.0182 $cm^2\ g^{-1}$ ('OH5 dust'; Ossenkopf & Henning 1994). The temperature of B35A has been estimated by Morgan et al. (2008) and Craigon (2015). Both studies found two distinct regimes within the cloud: a cold region ($T_{gas} = 10−20$ K, $T_{dust} = 18$ K) in the shielded cloud interior located to the east of the YSOs and a warm region ($T_{gas} = 20−30$K) to the west of the YSOs. Since the region where the YSOs are located lies close to the western edge of the warm cloud, a $T_{dust} = 25$ K was adopted to estimate the H_2 column density map illustrated in Fig. 5a based on Craigon (2015) and Reipurth & Friberg (2021). The H_2 column density towards the B35A sources is reported in Table 3. The error on the H_2 column density was estimated according to the 5% flux calibration uncertainty (Dempsey et al. 2013). It does not include the errors on T_{dust} due to the uncertainties on the upper and lower limits for T_{dust} in the YSO region.

Increasing the dust temperature to 30 K would lower the H_2 column density by 22% and consequently increase the abundance of the gas-phase species by the same amount; on the other hand, lowering the dust temperature to 18 K would increase the H_2 column density by 61% and consequently lower the gas abundance likewise. The above estimates assume an excitation temperature equal to 25 K for CO and CH_3OH. Increasing both
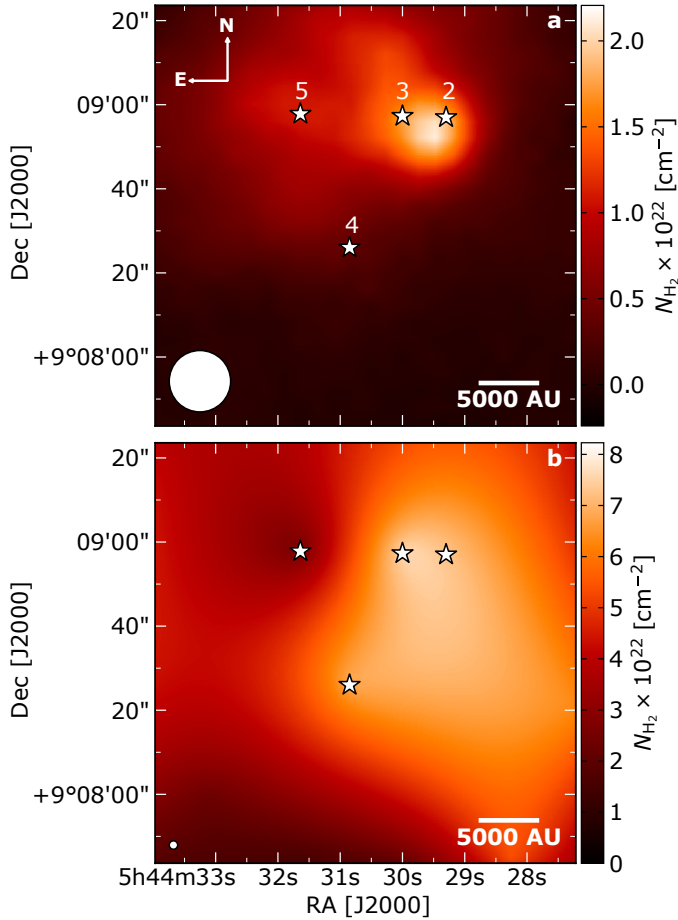
Fig. 5. H_2 column density maps of B35A. *a*: N_{H_2} map calculated from SCUBA−2 dust emission at 850 μm (Reipurth & Friberg 2021). *b*: N_{H_2} map calculated from the visual extinction. The synthesised beams are displayed in white in the bottom left corner of each panel. The white stars mark the positions of the targeted B35A sources.

the excitation temperature and the dust temperature to 30 K would result in gas abundances increasing by 24%. Conversely, lowering both temperatures to 18 K would lower the abundances by 33%. A comprehensive description of the production of the H_2 column density map from SCUBA−2 measurements is given in Appendix C of Perotti et al. (2020).

The H_2 column density map calculated from the SCUBA−2 measurements supplies an accurate estimate of the total beam-averaged amount of gas towards B35A, and therefore provides a useful reference for the optically thin gas-phase tracers. However, the derived H_2 column density map cannot be directly related to the AKARI data that supply (pencil-beam) measurements of the column densities towards the infrared sources that may or may not be embedded within the B35A cloud.

For the ice observations, the H_2 column density map was therefore obtained by performing a linear interpolation of the tabulated visual extinction (A_V) values for B35A taken from the *Spitzer* c2d catalogue[5] (see Appendix B). Since no calculated A_V values are reported for B35A−2 or B35A−3, the A_V for B35A−3 was acquired by de-reddening the spectral energy distribution (SED) at the 2MASS J, H, and K photometric points to fit a blackbody and using a second blackbody to model the infrared

excess at longer wavelengths. A detailed description of the fitting procedure adopted for B35A−3 is given in Appendix B. Following Evans et al. (2009) and Chapman et al. (2009), we adopted an extinction law for dense ISM gas with $R_V = 5.5$ from Weingartner & Draine (2001) to calculate A_V. The visual extinction for B35A−2 could not be estimated through a similar procedure due to the lack of NIR photometry data available for this object, and thus the A_V for this source was obtained through the interpolation of the available visual extinction measurements for B35A. The final A_V values of the four sources are listed in Table 1. Finally, the visual extinction was converted to H_2 column density using the relation $N_{H_2} = 1.37 \times 10^{21}$ cm^{-2} (A_V/mag), which was established for dense ISM gas (Evans et al. 2009). The H_2 column density calculated from the A_V map is shown in Fig. 5b.

The H_2 column densities calculated from both methods are of the same order of magnitude, 10^{22} cm^{-2} (Table 3). The column densities differ by approximately a factor of four, possibly due to variations in the exact column densities traced by SCUBA−2 and A_V measurements as well as assumptions on the dust temperature. In both H_2 column density maps (Figs. 5a,b), it is seen that the four sources lie in the densest region of the cloud, confirming the results previously presented in Craigon (2015) and Reipurth & Friberg (2021). Although the two maps were calculated using two different methods, they reproduce the same trend: B35A−2 and B35A−3 are located where the H_2 column density peaks, whereas B35A−4 and B35A−5 are situated in less dense regions. However, in the H_2 column density map calculated from the visual extinction (Fig. 5b), lower N_{H_2} values are reported for B35A−5 with respect to the other YSOs, whereas this is not the case in the H_2 column density map calculated from the SCUBA−2 map (Fig. 5a), where lower N_{H_2} values are observed for B35A−4. This difference can be explained by recalling that B35A−5 is the less extincted YSO ($A_V = 19.5$ mag) and is located along the trajectory of the giant outflow launched by B35A−3. Consequently, the SCUBA−2 observations (14.6″ beam) are likely tracing the more extended structure of the dust emission in the region and not resolving the more compact emission towards each individual object. It is worth recalling that embedded protostars and Herbig-Haro objects can substantially affect the dust emission morphology (Chandler & Carlstrom 1996); hence, the N_{H_2} enhancement seen in Fig. 5a likely reflects dust heating by the embedded protostars and by HH175, resulting in an increase in the sub-millimetre continuum flux rather than in a higher column density.

4. Analysis

4.1. Gas-ice maps

In Fig. 6 the distributions of gas-phase ^{13}CO 2−1 (panel a) and C^{18}O 2−1 (panel b) emissions are compared to CO ice abundances. Both CO isotopologue emissions are concentrated at the B35A−2, B35A−3, and B35A−5 source positions. The emission towards these three sources is of comparable intensity but drops in the surroundings of B35A−4, especially towards the southern edge of the cloud. The CO ice abundances with respect to H_2 are not characterised by large variations; instead, they are quite uniform and consistent within the uncertainties (Table 4). Only an upper limit could be determined for the CO ice column density towards B35A−5 due to the uncertainty in distinguishing the absorption feature at 3.53 μm in the spectrum of this object.

In Fig. 6c the distribution of gas-phase CH$_3$OH $5_0−4_0$ A$^+$ emission is compared to CH$_3$OH ice abundances. As described
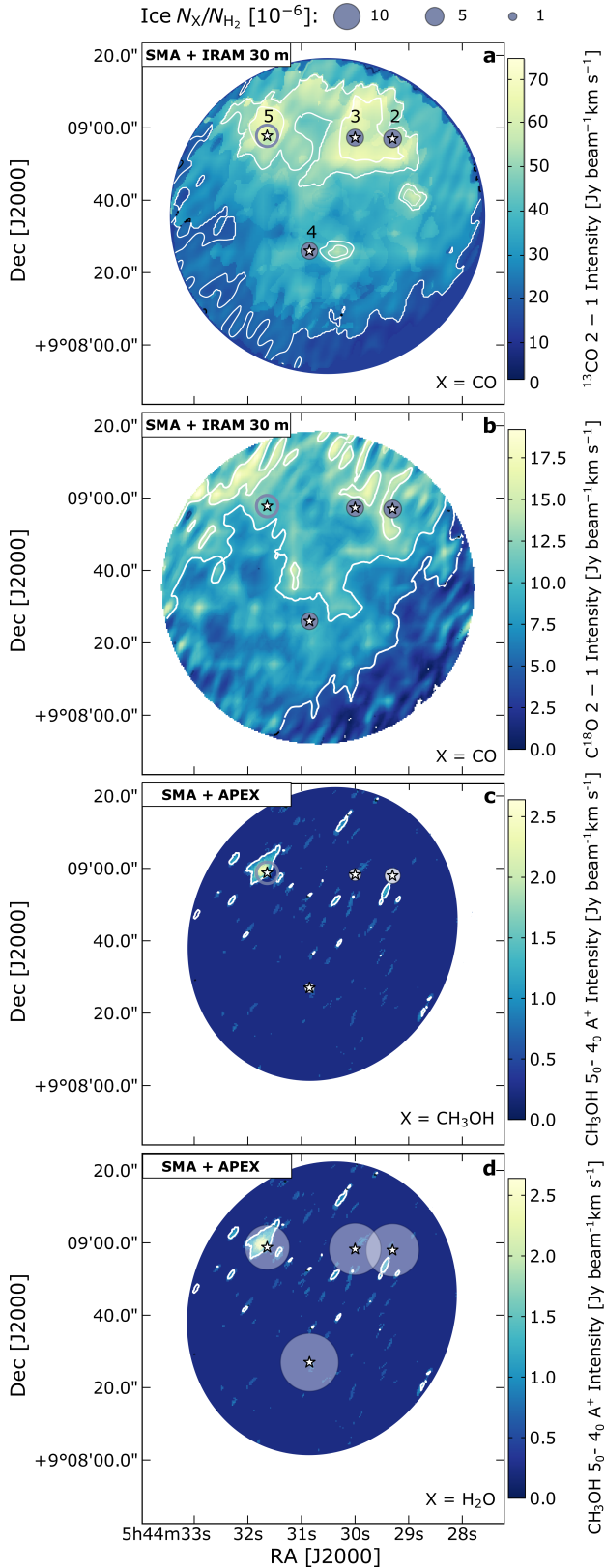
Fig. 6. Gas-ice maps of B35A. Ice abundances are indicated as filled grey (*panels a and b*) or white circles (*panels c and d*), and upper limits are displayed as empty circles. Contour levels are 5, 10, and 15σ. *a*: CO ice abundances on gas ^{13}CO 2−1. *b*: CO ice abundances on gas $C^{18}O$ 2−1. *c*: CH_3OH ice abundances on gas CH_3OH 5_0−4_0 A^+. *d*: H_2O ice abundances on gas CH_3OH 5_0−4_0 A^+. The white area outlines the primary beam of the SMA observations. The white stars mark the positions of the targeted B35A sources.

in Sect. 3.1, the CH_3OH emission is concentrated solely in one ridge, located in the proximity of the B35A−5 position. At this location, only an upper limit on the CH_3OH ice abundance could be determined. The morphology of the CH_3OH emission suggests that while B35A−5 is situated in a shocked region, sitting along the trajectory of the giant outflow, B35A−4 lies in a more quiescent area that is less influenced by high-velocity flows of matter. The CH_3OH ice abundances with respect to H_2 are characterised by slightly larger variations compared to CO ice (Table 4).

Finally, in Fig. 6d, the distribution of gas-phase CH_3OH 5_0−4_0 A^+ emission is compared to H_2O ice abundances. The H_2O ice abundances are approximately one order of magnitude higher than the CO and CH_3OH ice abundances (Table 4). The lowest H_2O ice abundance is reported towards B35A−5, where the CH_3OH peak emission is observed. In contrast, the highest H_2O ice abundance is obtained towards B35A−4, where CH_3OH emission is not detected.

4.2. Gas and ice variations

In Fig. 7 the search for gas-ice correlations towards B35A is addressed by analysing gas and ice abundances relative to H_2 (Table 4). The *y*-axes of all three panels display CO gas abundances, which are compared to abundances of CO ice (panel a), CH_3OH ice (panel b), and H_2O ice (panel c). To maintain gas and ice observations in their own reference frame, the CO gas abundances were estimated using N_{H_2} values calculated from SCUBA−2 850 μm maps, whereas the ice abundances were calculated using N_{H_2} values obtained from the visual extinction map (see Sect. 3.3 and Appendix B). The formalism adopted to propagate the uncertainty from the column densities to the abundances is reported in Appendix A.4.

It is immediately apparent that none of the ice species exhibit a predictable trend in ice abundance with gas abundance. Panels a and b show a similar behaviour since they are comparing molecules that are chemically linked: CO gas versus CO ice and CO gas versus CH_3OH ice, with CO being the precursor of CH_3OH. At the same time, panel c does not display the same relationships seen in the previous two panels. The latter observation is not surprising since there is no reason for CO and H_2O to be directly linked from a purely chemical perspective.

In both panels of Fig. 7, B35A−4 displays the highest CO gas and the lowest CO and CH_3OH ice abundances. When the uncertainties are taken into account, the CO ice abundances towards B35A−2, B35A−3, and B35A−4 are alike (Table 4). For the CH_3OH ice abundances, B35A−3 and B35A−4 are consistent within the error bars; only towards B35A−2 is a significant difference found. Both CO and CH_3OH ice abundances towards B35A−5 are upper limits (Table 4). The similarity between CO and CH_3OH ice trends and the fact that the CH_3OH/CO ice ratios are >0.3 indicate an efficient CH_3OH formation through CO hydrogenation (Watanabe & Kouchi 2002) on the grain surfaces of B35A. The CO gas abundances towards B35A−2, B35A−3, and B35A−5 are in agreement within the uncertainties (Table 4).

In panel c some of the gas-ice variations differ with respect to panels a and b: B35A−4 is characterised by the highest H_2O ice abundance, whereas B35A−5 shows the lowest H_2O ice abundance. This result corroborates the prediction that the ices of B35A−5 are the most depleted of volatile molecules among the B35A sources. The behaviours of B35A−2 and B35A−3 are similar if the uncertainties are considered (Table 4). The observed ice and gas variations between CO gas, CH_3OH gas, and H_2O ice towards B35A−4 and B35A−5 favour a scenario in which H_2O

Table 4. Ice and gas abundances relative to H_2 towards the B35A sources.

Object	$X_{H_2O}^{ice}$ [10^{-5}]	X_{CO}^{ice} [10^{-5}]	$X_{CH_3OH}^{ice}$ [10^{-5}]	$X_{^{12}CO}^{gas}$ [10^{-4}]	$X_{CH_3OH}^{gas}$ [10^{-8}]
B35A−2	4.10 ± 0.18	0.47 ± 0.04	0.36 ± 0.04	2.97 ± 0.63	...
B35A−3	3.99 ± 0.16	0.43 ± 0.04	0.21 ± 0.04	2.31 ± 0.49	...
B35A−4	4.93 ± 0.52	0.41 ± 0.50	0.15 ± 0.09	7.13 ± 1.50	...
B35A−5	2.93 ± 0.50	<0.68	<0.68	3.63 ± 0.76	1.75 ± 0.24

Notes. The column densities employed in the determination of the ice and gas abundances of H_2O, CO, and CH_3OH are listed in Table 3. The abundances of the gaseous species are obtained using $N_{H_2}^{SCUBA-2}$, whereas the abundances of the ice species are relative to $N_{H_2}^{A_V}$ (Table 3). Ellipses mark the non-detections of gas-phase CH_3OH.
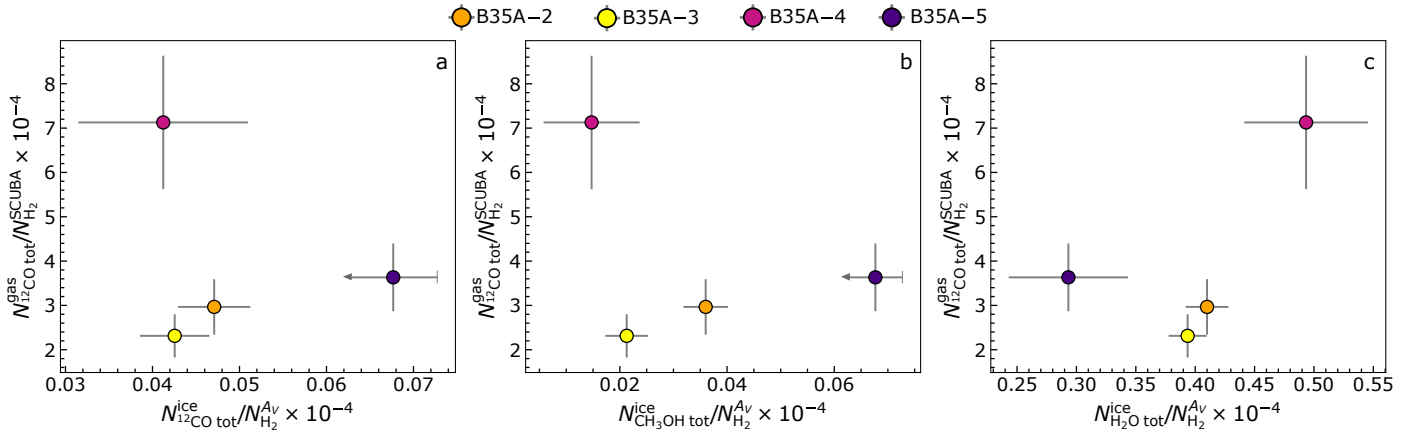
Fig. 7. Gas and ice variations in B35A. The circles represent the targeted B35A sources. *Panels a–c*: relation between CO, CH_3OH, and H_2O ice and CO gas abundances relative to H_2.

ice is formed and predominantly resides on the ices of B35A−4, likely located in the most 'quiescent' area of the targeted region, whereas in the proximity of a shocked region (B35A−5), H_2O ice mantles are partially desorbed. This result is discussed further in Sect. 5.1. Although the gas and ice variations analysed in this section and in Sect. 4.1 are based on a small sample, they still highlight interesting trends in accordance to what we would expect from our knowledge of the physical structure of the targeted region.

### 4.3. Comparison with previous gas-ice maps of B35A

Noble et al. (2017) produced the first gas-ice maps of B35A. They compared AKARI ice abundances from Noble et al. (2013) with: single-dish (JCMT/HARP and IRAM 30 m/HERA) gas-phase maps of $C^{18}O$ (Buckle et al. 2009; Craigon 2015; $J = 3–2$ and $2–1$), sub-millimetre continuum SCUBA maps at 850 μm and 450 μm/850 μm (Di Francesco et al. 2008), and *Herschel*/SPIRE maps at 250 μm (Griffin et al. 2010). The H_2 gas-phase map adopted to calculate ice abundances was determined from CO observations (Craigon 2015).

Noble et al. (2013, 2017) derived their ice column densities without considering the presence of CH_3OH, and thus the H_2O ice column densities were routinely higher than those used here from Suutarinen (2015; our Fig. 8). Simultaneously, the CO ice column densities were calculated using different laboratory data; for example, the CO-ice red component was fitted using a CO:H_2O (Fraser & van Dishoeck 2004) laboratory spectrum as opposite to the CO:CH_3OH mixture (Cuppen et al. 2011),

resulting in a higher CO-ice column density compared to Suutarinen (2015).

The combination of gas, dust, and ice observations proposed in Noble et al. (2017) is characterised by a number of limitations that are taken into account in the presented work, including: the lower angular resolution of the adopted single-dish observations, the analysis of the chemical behaviours of only simple molecules (e.g. H_2O, CO, and CO_2), and not taking into account the fact that the ice and gas observations might probe different depths. The presented work overcomes these limitations by making use of higher angular resolution interferometric observations, studying the ice and gas variations of both simple (H_2O, CO) and complex molecules (CH_3OH), and, lastly, by comparing ice and gas abundances derived using two different H_2 column density maps (to keep the ice and gas observations in their own reference frame).

From the analysis of the gas-ice maps, Noble et al. (2017) inferred that the dust in B35A is mainly localised around B35A−2 and B35A−3, in agreement with the higher ice column densities of H_2O and CO towards these two sources (Fig. 8). However, they observed that the H_2O ice column densities are lower towards B35A−5 compared to B35A−4, even though the dust emission is higher towards B35A−5. The authors conclude that no clear trend between ice, dust, and gas is seen in B35A and that more knowledge of the local-scale astrophysical environment is needed to disentangle the exact interplay between ice and gas in the region. The findings of Noble et al. (2017) are in agreement with the observational results and the gas-ice maps of B35A presented here (with the caveat that both
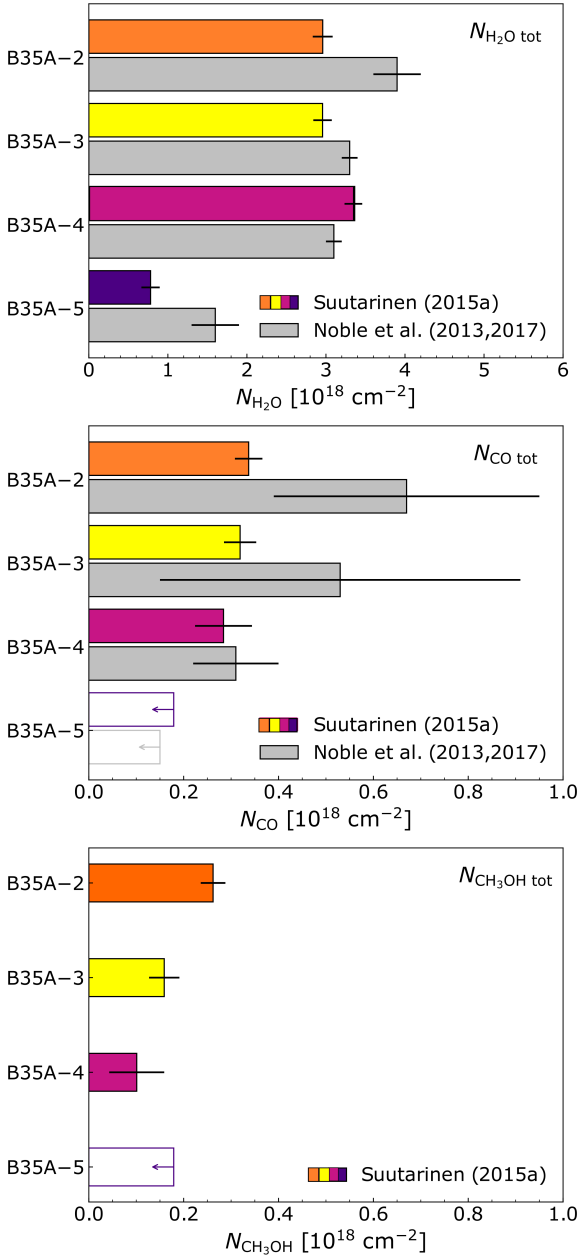
Fig. 8. H$_2$O (*top*), CO (*middle*), and CH$_3$OH (*bottom*) total ice column densities obtained in Suutarinen (2015, the sources are colour-coded) compared to Noble et al. (2017, light grey). The empty bars represent upper limits on the column densities.

CO ice abundances towards B35A−5 in Noble et al. 2017 and in this work are upper limits). However, the gas-ice maps produced in this study show that the lower H$_2$O ice abundance towards B35A−5 compared to B35A−4 is plausibly caused by the influence of shocks on the ice chemistry. CH$_3$OH is a tracer of energetic inputs in the form of outflows (Kristensen et al. 2010; Suutarinen et al. 2014), and it traces the trajectory of the bipolar outflow in B35A. As a result, lower H$_2$O ice abundances towards B35A−5 are likely the result of sputtering effects in the outflow shocks (e.g. Suutarinen et al. 2014 and references therein). Simultaneously, the fact that the sub-millimetre dust emission towards B35A−5 is high where the H$_2$O ice abundances are lower can also be explained by the presence of the outflow terminating at the Herbig-Haro object HH 175. In fact,

UV radiation generated in the Herbig-Haro object itself may locally heat the dust, enhancing the sub-millimetre continuum flux of the region (Chandler & Carlstrom 1996; Kristensen et al. 2010; Fig. 5a).

5. Discussion

The CH$_3$OH gas abundances in B35A (10^{-8}) are greater than what could be inferred by pure gas-phase synthesis (e.g. Garrod et al. 2006). Hence, the observed CH$_3$OH gas must be produced on the grain surfaces and be desorbed afterwards. In the following, the preferred scenario for CH$_3$OH desorption in B35A is discussed. Additionally, the observational results presented in Sects. 3.1−3.2 are employed to determine CH$_3$OH and CO gas-to-ice ratios (N_{gas}/N_{ice}) towards the multiple protostellar system in B35A. Finally, a comparison between the gas-to-ice ratios directly determined towards B35A and the gas-to-ice ratios of nearby star-forming regions is proposed.

5.1. Sputtering of CH$_3$OH in B35A

Sections 3.1 and 4.1 showed that the CH$_3$OH emission is concentrated almost exclusively in one ridge, which coincides with the B35A−5 position. B35A−5 sits along the eastern lobe of a large collimated outflow emanated from the binary Class I IRAS 05417+0907 (i.e. B35A−3). The eastern lobe has a total extent of 0.6 pc, and it terminates at the Herbig-Haro object HH 175 (Craigon 2015). The total extent of the outflow is 1.65 pc (Reipurth & Friberg 2021), which places HH 175 among the several dozen Herbig-Haro objects with parsec dimensions (Reipurth & Bally 2001). Herbig-Haro objects are omnipresent in star-forming regions, but it is still not clear how exactly they are tied into the global star-formation process, for example how they alter the morphology and kinematics of the gas in which they originate. These are highly energetic phenomena that are believed to form when high-velocity protostellar jets collide with the surrounding molecular cloud, inducing shocks. Such shocks compress and heat the gas, generating UV radiation (Neufeld & Dalgarno 1989). The activity of Herbig-Haro objects can dramatically change the chemical composition of the gas in their vicinity, mutating the chemistry of the region during so-called sputtering processes (Neufeld & Dalgarno 1989; Hollenbach & McKee 1989).

Sputtering takes place in shocks when neutral species (e.g. H$_2$, H, or He) collide with the surface of ice-covered dust grains with sufficient kinetic energy to expel ice species (e.g. CH$_3$OH, NH$_3$, or H$_2$O) into the gas phase (Jørgensen et al. 2004; Jiménez-Serra et al. 2008; Kristensen et al. 2010; Suutarinen et al. 2014; Allen et al. 2020). During a sputtering event, the ice molecules can desorb intact or be destroyed (e.g. via dissociative desorption) either due to the high kinetic energy or by reactions with H atoms (Blanksby & Ellison 2003; Dartois et al. 2019, 2020). The fragments of dissociated molecules can then readily recombine in the gas phase (Suutarinen et al. 2014 and references therein).

The inferred dust temperatures in the B35A region (20−30 K) are remarkably lower than the CH$_3$OH sublimation temperature (∼128 K; Penteado et al. 2017), which rules out thermal desorption as a potential mechanism triggering the observed CH$_3$OH emission. This consideration, together with the observation of the CH$_3$OH emission along the HH 175 flow direction and the anti-correlation between CH$_3$OH emission and the lower H$_2$O ice abundances towards B35A−5, suggests that ice sputtering in shock waves is a viable mechanism to desorb
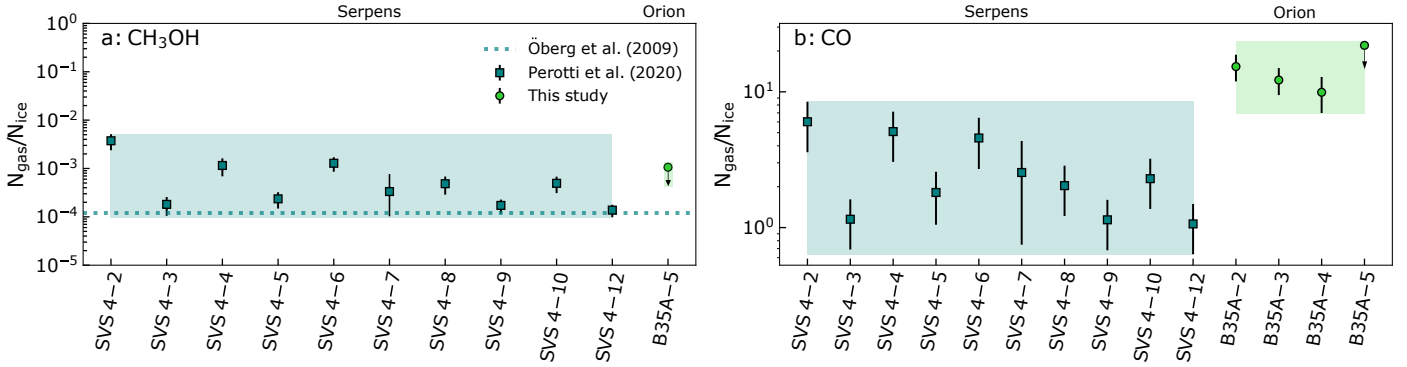
Fig. 9. CH$_3$OH (*panel a*) and CO (*panel b*) gas-to-ice ratios (N_{gas}/N_{ice}) for the multiple protostellar system in Orion B35A and Serpens SVS 4. The dark green squares indicate the gas-to-ice ratios estimated by Perotti et al. (2020) for the Serpens SVS 4 cluster. The light green circles mark the ratios calculated in this study. The dotted light blue line in *panel a* represents the ratio estimated by Öberg et al. (2009) towards Class 0/I objects. The shaded areas indicate the estimated ranges of the gas-to-ice ratios.

ice molecules in B35A. Simultaneously, the absence of shocks towards B35A−4 likely explains the highest abundance of H$_2$O ice observed in this more quiescent region (Fig. 6d). Higher angular resolution observations of CH$_3$OH in the region are required to provide quantitative measurements of the amount of CH$_3$OH desorbed via sputtering compared to other non-thermal desorption mechanisms. Additional gas-phase observations of H$_2$O towards the B35A sources are needed to further constrain the processes linking H$_2$O ice and H$_2$O gas in this shocked region (e.g. sputtering of H$_2$O ice mantles versus direct H$_2$O gas-phase synthesis) and, in a broader context, to help explain the high abundances of H$_2$O observed in molecular outflows (Nisini et al. 2010; Bjerkeli et al. 2012, 2016; Santangelo et al. 2012; Vasta et al. 2012; Dionatos et al. 2013).

5.2. Gas-to-ice ratios

Figure 9 displays the CH$_3$OH (panel a) and CO (panel b) gas-to-ice ratios towards ten sources constituting the SVS 4 cluster located in the Serpens molecular cloud (Perotti et al. 2020) and towards the B35A sources in the Orion molecular cloud. The shaded areas indicate the estimated ranges of gas-to-ice ratios towards both molecular clouds, providing complementary information about the gas-to-ice ratios of both regions compared to the value calculated towards each individual source.

Figure 9a shows the CH$_3$OH gas-to-ice ratios ($N_{CH_3OH_{gas}}/N_{CH_3OH_{ice}}$) towards the SVS 4 sources and B35A−5. Only an upper limit for the CH$_3$OH gas-to-ice towards B35A−5 is obtained (i.e. 1.1×10^{-3}) due to the uncertainty on the CH$_3$OH ice column density determination towards this source (Suutarinen 2015). Therefore, only limited information is available regarding the CH$_3$OH chemistry in B35A. Figure 9a also displays the averaged CH$_3$OH gas-to-ice ratio towards four low-mass embedded protostars located in nearby star-forming regions from Öberg et al. (2009). A detailed comparison between the CH$_3$OH gas-to-ice ratios for the SVS 4 cluster members and the value estimated by Öberg et al. (2009) is given in Perotti et al. (2020) and therefore not repeated here.

The observations of B35A address cold quiescent CH$_3$OH emission ($J = 5_K−4_K$ transitions at 241.7 GHz and E_u from 34.8 to 60.7 K; see Table 2) and presumably quiescent gas not affected by outflow shocks and/or thermally desorbed in the vicinity of the protostar. The same applies to the observations presented in Öberg et al. (2009; $J = 2−1$ transitions at 96.7 GHz and E_u in the range 14.4−35.4 K). However, B35A−5 and the SVS 4 sources that report the highest gas-to-ice ratios are likely affected to some

extent by outflow shocks (i.e. B35A−5 by the giant outflow terminating at HH 175 and the SVS 4 sources by the outflow known to be associated with SMM 4). This might justify the mismatch between the Öberg et al. (2009) value and the higher values of the gas-to-ice ratios. In the case of the B35A cloud, high-sensitivity infrared observations of B35A are required to further constrain this observation.

CO gas-to-ice ratios ($N_{CO_{gas}}/N_{CO_{ice}}$) towards the SVS 4 and B35A sources are illustrated in Fig. 9b. As discussed previously in Perotti et al. (2020), the range of gas-to-ice ratios for SVS 4 extends between one and six, and it is significantly higher than the predicted value ($\sim 4 \times 10^{-2}$; Cazaux et al. 2016). This theoretical prediction is estimated from the three-phase astrochemical model by Cazaux et al. (2016), which includes thermal and non-thermal desorption processes of the species constituting the ice mantles. This comparison with the theoretical prediction has to be taken with care since the physical model is not specifically tuned to reproduce the structures of the SVS 4 cluster or the B35A cloud. The estimated dust temperature towards the SVS 4 cluster is below 20 K (Kristensen et al. 2010), indicating that CO is likely frozen out on the grain surfaces. We concluded from the high relative CO gas abundances that the gas-mapping does not trace the densest regions of the SVS 4 cluster but rather an extended component that is not sensitive to the effects of freeze-out (Fig. 8 of Perotti et al. 2020).

High CO gas-to-ice ratios are also observed for B35A, but in this case they are mainly attributable to CO that is thermally desorbed in the region. The physical conditions of B35A and SVS 4 differ significantly; for example, the western side of B35A is highly influenced by the ionisation-shock front driven by the λ Orionis OB stars, and the dust temperature in the YSO region of B35A has been estimated to be at least 25−30 K (Craigon 2015; Morgan et al. 2008). Therefore, at these temperatures, which are above the CO sublimation temperature (~ 20 K; Bisschop et al. 2006; Collings et al. 2004; Acharyya et al. 2007), CO is efficiently thermally desorbed from the grain surfaces and is expected to primarily reside in the gas phase. According to this result, the observed CH$_3$OH ice might have formed at earlier stages, prior to the warming of the dust grains, or, alternatively, from CO molecules trapped in porous H$_2$O matrices, and is therefore not sublimated at these temperatures. Additionally, higher abundances of CO might reflect an active CO gas-phase synthesis in the region. Follow-up observations of higher J transitions of CO isotopologues are required to provide a conclusive assessment.

6. Conclusions

Millimetric (SMA, APEX, IRAM 30 m) and infrared (AKARI) observations were used to investigate the relationships between ice, dust, and gas in the B35A cloud, which is associated with the λ Orionis region. Gas and ice maps were produced to compare the distribution of solid (H_2O, CO, and CH_3OH) and gaseous (^{13}CO, $C^{18}O$, and CH_3OH) molecules and to link the small-scale variations traced by ice observations with the larger-scale astrophysical phenomena probed by gas observations. The main conclusions are as follows.

– The CO isotopologue emission is extended in B35A, whereas the observed CH_3OH emission is compact and centred in the vicinity of B35A−5. B35A−5 sits along the trajectory of the outflow emanated from IRAS 05417+0907 (i.e. B35A−3), and thus the observed gas-phase CH_3OH can plausibly be explained by the sputtering of ice CH_3OH in the outflow shocks.

– The dust column density traced by the sub-millimetre emission is not directly related to the ice column inferred from the infrared observations. The sub-millimetre dust emission is stronger towards B35A−2, B35A−3, and B35A−5 compared to B35A−4; however, the H_2O ice column density is higher for B35A−4. This discrepancy is understood by taking into account the fact that B35A−2, B35A−3, and B35A−5 are situated in a shocked region that is affected by the presence of the Herbig-Haro object HH175 – and thus likely influenced by sputtering and heating affecting the observed sub-millimetre dust emission pattern.

– None of the ice species show a predictable trend in ice abundance with gas-phase abundance. This implies that inferring ice abundances from known gas-phase abundances and vice versa is inaccurate without an extensive knowledge of the physical environment of the targeted region.

– The high CO gas-to-ice ratios suggest that the CO molecules are efficiently thermally desorbed in B35A. This is supported by dust temperature estimates (25−30 K) towards the B35A sources that are above the CO sublimation temperature (∼20 K).

– Simultaneously, the dust temperatures in the region are significantly lower than the CH_3OH sublimation temperature (128 K), ruling out thermal desorption as the mechanism responsible for the observed CH_3OH emission.

– The combination of gas and ice observations is essential for comprehending the relationships at the interface between solid and gas phases, and hence for linking the small-scale variations detected in the ice observations with the large-scale phenomena revealed by gas-phase observations.

The presented work is a preparatory study for future combined *James Webb* Space Telescope (JWST) and Atacama Large Millimeter/submillimeter Array (ALMA) observations, which will shed further light on the dependences of gas-to-ice ratios on the physical conditions of star-forming regions. In fact, future mid-infrared facilities, notably JWST, will considerably increase the number of regions for which ice maps are available. Such high-sensitivity ice maps can then be combined with ALMA observations to provide better constraints on the complex interplay between ice, dust, and gas during the earliest phases of star formation. The present study already shows that such gas-ice maps will be valuable given that they probe ice- and gas-phase chemistries to a greater extent than ice or gas maps alone.

References

Acharyya, K., Fuchs, G. W., Fraser, H. J., van Dishoeck, E. F., & Linnartz, H. 2007, A&A, 466, 1005
Allen, V., Cordiner, M., & Charnley, S. 2020, ArXiv e-prints [arXiv:2010.01151]
Ansdell, M., Haworth, T. J., Williams, J. P., et al. 2020, AJ, 160, 248
Barnes, P. J., Muller, E., Indermuehle, B., et al. 2015, ApJ, 812, 6
Barrado, D., Stelzer, B., Morales-Calderón, M., et al. 2011, A&A, 526, A21
Barrado, D., de Gregorio Monsalvo, I., Huélamo, N., et al. 2018, A&A, 612, A79
Bayo, A., Barrado, D., Stauffer, J., et al. 2011, A&A, 536, A63
Bergin, E. A., & Tafalla, M. 2007, ARA&A, 45, 339
Bergner, J. B., Öberg, K. I., Garrod, R. T., & Graninger, D. M. 2017, ApJ, 841, 120
Bertin, M., Romanzin, C., Doronin, M., et al. 2016, ApJ, 817, L12
Bisschop, S. E., Fraser, H. J., Öberg, K. I., van Dishoeck, E. F., & Schlemmer, S. 2006, A&A, 449, 1297
Bjerkeli, P., Liseau, R., Larsson, B., et al. 2012, A&A, 546, A29
Bjerkeli, P., Jørgensen, J. K., Bergin, E. A., et al. 2016, A&A, 595, A39
Blanksby, S., & Ellison, G. 2003, Acc. Chem. Res., 36, 255
Boogert, A. C. A., Gerakines, P. A., & Whittet, D. C. B. 2015, ARA&A, 53, 541
Buckle, J. V., Hills, R. E., Smith, H., et al. 2009, MNRAS, 399, 1026
Calcutt, H., Jørgensen, J. K., Müller, H. S. P., et al. 2018, A&A, 616, A90
Carlhoff, P., Nguyen Luong, Q., Schilke, P., et al. 2013, A&A, 560, A24
Cazaux, S., Tielens, A. G. G. M., Ceccarelli, C., et al. 2003, ApJ, 593, L51
Cazaux, S., Minissale, M., Dulieu, F., & Hocuk, S. 2016, A&A, 585, A55
Cazaux, S., Martín-Doménech, R., Chen, Y. J., Muñoz Caro, G. M., & González Díaz C. 2017, ApJ, 849, 80
Chandler, C. J., & Carlstrom, J. E. 1996, ApJ, 466, 338
Chapman, N. L., Mundy, L. G., Lai, S.-P., & Evans, II, N. J. 2009, ApJ, 690, 496
Collings, M. P., Anderson, M. A., Chen, R., et al. 2004, MNRAS, 354, 1133
Connelley, M. S., Reipurth, B., & Tokunaga, A. T. 2008, AJ, 135, 2496
Conti, P. S., & Leep, E. M. 1974, ApJ, 193, 113
Craigon, A. M. 2015, PhD thesis, University of Strathclyde, UK
Cruz-Diaz, G. A., Martín-Doménech, R., Muñoz Caro, G. M., & Chen, Y.-J. 2016, A&A, 592, A68
Cuppen, H. M., Penteado, E. M., Isokoski, K., van der Marel, N., & Linnartz, H. 2011, MNRAS, 417, 2809
Dartois, E., Chabot, M., Id Barkach, T., et al. 2019, A&A, 627, A55
Dartois, E., Chabot, M., Bacmann, A., et al. 2020, A&A, 634, A103
De Vries, C. H., Narayanan, G., & Snell, R. L. 2002, ApJ, 577, 798
Dempsey, J. T., Friberg, P., Jenness, T., et al. 2013, MNRAS, 430, 2534
Di Francesco, J., Johnstone, D., Kirk, H., MacKenzie, T., & Ledwosinska, E. 2008, ApJS, 175, 277
Dionatos, O., Jørgensen, J. K., Green, J. D., et al. 2013, A&A, 558, A88
Dolan, C. J., & Mathieu, R. D. 1999, AJ, 118, 2409
Dolan, C. J., & Mathieu, R. D. 2002, AJ, 123, 387
Dulieu, F., Congiu, E., Noble, J., et al. 2013, Sci. Rep., 3, 1338
Eistrup, C., Walsh, C., & van Dishoeck, E. F. 2016, A&A, 595, A83
Evans, II, N. J., Dunham, M. M., Jørgensen, J. K., et al. 2009, ApJS, 181, 321
Evans, II, N. J., Allen, L. E., Blake, G. A., et al. 2014, VizieR Online Data Catalog: II/332
Fraser, H. J., & van Dishoeck, E. F. 2004, Adv. Space Res., 33, 14

Fraser, H. J., Collings, M. P., McCoustra, M. R. S., & Williams, D. A. 2001, MNRAS, 327, 1165
Garrod, R., Park, I. H., Caselli, P., & Herbst, E. 2006, Faraday Discuss., 133, 51
Goldsmith, P. F., & Langer, W. D. 1999, ApJ, 517, 209
Grassi, T., Bovino, S., Caselli, P., et al. 2020, A&A, 643, A155
Griffin, M. J., Abergel, A., Abreu, A., et al. 2010, A&A, 518, L3
Güsten, R., Nyman, L. Å., Schilke, P., et al. 2006, A&A, 454, L13
Heiles, C., & Habing, H. J. 1974, A&AS, 14, 1
Herbst, E., & van Dishoeck, E. F. 2009, ARA&A, 47, 427
Hernández, J., Calvet, N., Hartmann, L., et al. 2009, ApJ, 707, 705
Ho, P. T. P., Moran, J. M., & Lo, K. Y. 2004, ApJ, 616, L1
Hollenbach, D., & McKee, C. F. 1989, ApJ, 342, 306
Jiménez-Serra, I., Caselli, P., Martín-Pintado, J., & Hartquist, T. W. 2008, A&A, 482, 549
Jørgensen, J. K., Hogerheijde, M. R., Blake, G. A., et al. 2004, A&A, 415, 1021
Jørgensen, J. K., van der Wiel, M. H. D., Coutens, A., et al. 2016, A&A, 595, A117
Jørgensen, J. K., Belloche, A., & Garrod, R. T. 2020, ARA&A, 58, 727
Kauffmann, J., Bertoldi, F., Bourke, T. L., Evans, II, N. J., & Lee, C. W. 2008, A&A, 487, 993
Kounkel, M. 2020, ApJ, 902, 122
Kounkel, M., Covey, K., Suárez, G., et al. 2018, AJ, 156, 84
Kristensen, L. E., van Dishoeck, E. F., van Kempen, T. A., et al. 2010, A&A, 516, A57
Lada, C. J., & Black, J. H. 1976, ApJ, 203, L75
Ladd, E. F., Fuller, G. A., & Deane, J. R. 1998, ApJ, 495, 871
Lang, W. J., Masheder, M. R. W., Dame, T. M., & Thaddeus, P. 2000, A&A, 357, 1001
Lee, H.-T., Chen, W. P., Zhang, Z.-W., & Hu, J.-Y. 2005, ApJ, 624, 808
Maddalena, R. J., & Morris, M. 1987, ApJ, 323, 179
Manigand, S., Jørgensen, J. K., Calcutt, H., et al. 2020, A&A, 635, A48
Martín-Doménech, R., Muñoz Caro, G. M., & Cruz-Díaz, G. A. 2016, A&A, 589, A107
Mathieu, R. D. 2008, ASP Monographs, 4, 757
McGuire, B. A. 2018, ApJS, 239, 17
McMullin, J. P., Waters, B., Schiebel, D., Young, W., & Golap, K. 2007, ASP Conf. Ser., 376, 127
Morgan, L. K., Thompson, M. A., Urquhart, J. S., & White, G. J. 2008, A&A, 477, 557
Müller, H. S. P., Thorwirth, S., Roth, D. A., & Winnewisser, G. 2001, A&A, 370, L49
Murdin, P., & Penston, M. V. 1977, MNRAS, 181, 657
Myers, P. C., Linke, R. A., & Benson, P. J. 1983, ApJ, 264, 517
Myers, P. C., Heyer, M., Snell, R. L., & Goldsmith, P. F. 1988, ApJ, 324, 907
Neufeld, D. A., & Dalgarno, A. 1989, ApJ, 340, 869
Nisini, B., Benedettini, M., Codella, C., et al. 2010, A&A, 518, L120
Noble, J. A., Congiu, E., Dulieu, F., & Fraser, H. J. 2012, MNRAS, 421, 768

Noble, J. A., Fraser, H. J., Aikawa, Y., Pontoppidan, K. M., & Sakon, I. 2013, ApJ, 775, 85
Noble, J. A., Fraser, H. J., Pontoppidan, K. M., & Craigon, A. M. 2017, MNRAS, 467, 4753
Öberg, K. I. 2016, Chem. Rev., 116, 9631
Öberg, K. I., & Bergin, E. A. 2021, Phys. Rep., 893, 1
Öberg, K. I., Bottinelli, S., & van Dishoeck, E. F. 2009, A&A, 494, L13
Öberg, K. I., Murray-Clay, R., & Bergin, E. A. 2011, ApJ, 743, L16
Ossenkopf, V., & Henning, T. 1994, A&A, 291, 943
Penteado, E. M., Walsh, C., & Cuppen, H. M. 2017, ApJ, 844, 71
Perotti, G., Rocha, W. R. M., Jørgensen, J. K., et al. 2020, A&A, 643, A48
Pickett, H. M., Poynter, R. L., Cohen, E. A., et al. 1998, J. Quant. Spectr. Rad. Transf, 60, 883
Qin, S.-L., & Wu, Y.-F. 2003, Chinese J. Astron. Astrophys., 3, 69
Rabli, D., & Flower, D. R. 2010, MNRAS, 406, 95
Reipurth, B. 2000, VizieR Online Data Catalog: V/104
Reipurth, B., & Bally, J. 2001, ARA&A, 39, 403
Reipurth, B., & Friberg, P. 2021, MNRAS, 501, 5938
Sahan, M., & Haffner, L. M. 2016, AJ, 151, 147
Santangelo, G., Nisini, B., Giannini, T., et al. 2012, A&A, 538, A45
Schöier, F. L., van der Tak, F. F. S., van Dishoeck, E. F., & Black, J. H. 2005, A&A, 432, 369
Sharpless, S. 1959, ApJS, 4, 257
Skrutskie, M. F., Cutri, R. M., Stiening, R., et al. 2006, AJ, 131, 1163
Suutarinen, A. 2015, PhD thesis, The Open University, UK
Suutarinen, A. N., Kristensen, L. E., Mottram, J. C., Fraser, H. J., & van Dishoeck, E. F. 2014, MNRAS, 440, 1844
van Dishoeck, E. F., & Blake, G. A. 1998, ARA&A, 36, 317
van 't Hoff, M. L. R., Walsh, C., Kama, M., Facchini, S., & van Dishoeck, E. F. 2017, A&A, 599, A101
van Gelder, M. L., Tabone, B., Tychoniec, Ł., et al. 2020, A&A, 639, A87
Vasta, M., Codella, C., Lorenzani, A., et al. 2012, A&A, 537, A98
Vasyunin, A. I., & Herbst, E. 2013, ApJ, 769, 34
Wade, C. M. 1957, AJ, 62, 148
Watanabe, N., & Kouchi, A. 2002, ApJ, 571, L173
Weingartner, J. C., & Draine, B. T. 2001, ApJ, 548, 296
Whittet, D. C. B., Cook, A. M., Herbst, E., Chiar, J. E., & Shenoy, S. S. 2011, ApJ, 742, 28
Wilson, T. L. 1999, Rep. Prog. Phys., 62, 143
Wilson, T. L., & Matteucci, F. 1992, A&ARv, 4, 1
Wolfire, M. G., Hollenbach, D., & Tielens, A. G. G. M. 1989, ApJ, 344, 770
Yang, B., Stancil, P. C., Balakrishnan, N., & Forrey, R. C. 2010, ApJ, 718, 1062
Zhang, C. Y., Laureijs, R. J., Chlewicki, G., Clark, F. O., & Wesselius, P. R. 1989, A&A, 218, 231
Zhang, Z.-Y., Romano, D., Ivison, R. J., Papadopoulos, P. P., & Matteucci, F. 2018, Nature, 558, 260
Zucker, C., Speagle, J. S., Schlafly, E. F., et al. 2019, ApJ, 879, 125
Zucker, C., Speagle, J. S., Schlafly, E. F., et al. 2020, A&A, 633, A51

Appendix A: Production of gas-phase maps

A.1. Interferometric and single-dish data combination

The combined interferometric (SMA) and single-dish (APEX/IRAM 30 m) data were obtained using CASA version 5.6.1 by executing the CASA task `feather`. The `feathering` algorithm consists of Fourier transforming and scaling the single-dish (lower resolution) data to the interferometric (higher resolution) data. In a second step, the two datasets with different spatial resolutions are merged. In this work, APEX short spacing was used to correct the CH_3OH emission detected by SMA observations, whereas the IRAM 30 m short spacing was folded into the CO isotopologue emissions observed with the SMA. The combination of the interferometric and single-dish datasets was carried out following the procedure described in Appendix B.1 of Perotti et al. (2020) and references therein.

Artefacts might arise when combining interferometric and single-dish data. To benchmark our results, we varied the arguments of the feathering algorithm – for example `sdfactor` (scale factor to apply to single-dish images), `effdishdiam` (new effective single-dish diameter), and `lowpassfiltersd` (filtering out the high spatial frequencies of the single-dish image) – from the default values. The variations in the above parameters resulted in amplifying the signal close to the primary beam edges by approximately 15%, and therefore the default values were chosen.

### A.2. Optical depth of the CO isotopologues

If the emission of the ^{13}CO and $C^{18}O$ isotopologues is co-spatial, the line profiles are similar, and the gas ratio abundance $^{12}CO{:}^{13}CO{:}C^{18}O$ is constant, then the ^{13}CO optical depth can be assessed from the ^{13}CO and $C^{18}O$ integrated intensity ratio $I(^{13}CO)/I(C^{18}O)$ using the formalism first described by Myers et al. (1983) and Ladd et al. (1998). The treatment employed here is adapted from Myers et al. (1983) and uses Eq. (A.1) (given by e.g. Carlhoff et al. 2013; Zhang et al. 2018), which relates the integrated intensity ratio of the two isotopologues (Table A.1) and the optical depth τ:

$$\frac{I(^{13}CO)}{I(C^{18}O)} \approx \frac{1 - \exp(-\tau^{13CO})}{1 - \exp(-\tau^{13CO}/f)}. \tag{A.1}$$

In the above equation τ^{13CO} is the ^{13}CO optical depth and f is the intrinsic $^{13}CO/C^{18}O$ abundance ratio, which is equal to $7-10$ for the Milky Way (Wilson & Matteucci 1992; Barnes et al. 2015). If $f = 8$ is assumed, to be consistent with the approach adopted in Perotti et al. (2020), τ^{13CO} is equal to 1.22 for B35A−2, 0.39 for B35−3, 0.47 for B35A−5, and 0.03 for B35−4, indicating ^{13}CO optically thick emission towards three (B35A−2, B35−3, and B35A−5) out of four sources in the B35A cloud as $I(^{13}CO)/I(C^{18}O)$ is below the intrinsic ratio f for these three sources. The same conclusion is obtained if $f = 7$ or $f = 10$ is assumed. Based on this result, the $C^{18}O$ emission was used to estimate the column densities of ^{12}CO under LTE conditions.

A.3. Channel maps and spectra of individual transitions

Channel maps and spectra for the ^{13}CO $J = 2-1$, $C^{18}O$ $J = 2-1$, and CH_3OH $J = 5_0-4_0$ A^+ detected in the combined interferometric (SMA) and single-dish (IRAM 30 m/APEX) data are displayed in Figs. A.1 and A.3–A.5. The CO isotopologue emission is predominantly concentrated towards B35A−2 and
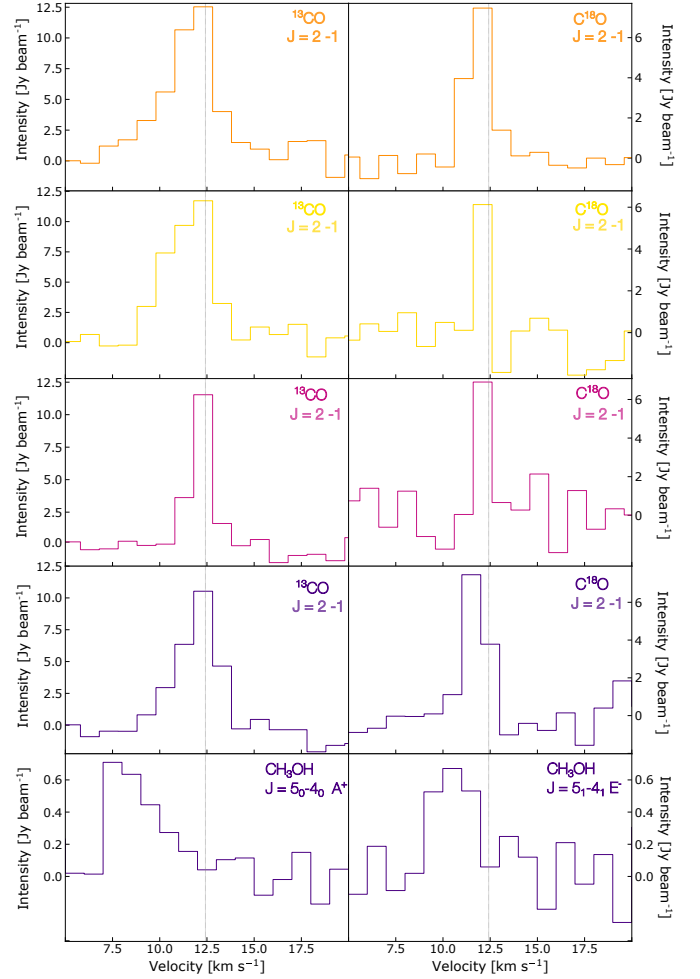
Fig. A.1. ^{13}CO $J = 2-1$, $C^{18}O$ $J = 2-1$, CH_3OH $J = 5_0-4_0$ A^+, and CH_3OH $J = 5_1-4_1$ E^- spectra towards the B35A sources detected in the combined interferometric and single-dish datasets. The spectra are colour-coded according to Fig. 7. The cloud velocity (12.42 km s^{-1}) is shown in all spectra with a vertical grey line.

Table A.1. Integrated ^{13}CO and $C^{18}O$ line intensities in units of Jy beam^{-1} km s^{-1} over each source position.

| Source	^{13}CO ($J = 2-1$)	$C^{18}O$ ($J = 2-1$)
B35A−2	70.64 ± 10.59	14.18 ± 2.86
B35A−3	72.36 ± 10.85	10.66 ± 2.17
B35A−4	59.63 ± 8.95	7.55 ± 1.56
B35A−5	70.74 ± 10.61	10.75 ± 2.19

B35A−3, whereas the CH_3OH emission is uniquely localised in the vicinity of B35A−5. Blue-shifted components are observed in combination with broad spectral profiles and wings that deviate from the cloud velocity (12.42 km s^{-1}).

A.4. Derivation of gas-phase column densities

The column densities of gas-phase species towards the B35A sources were calculated using the integrated intensities of the combined interferometric (SMA) and single-dish (IRAM 30 m/APEX) data (Tables A.1 and A.2). The values inserted into the equations below are listed in Table 2 and have

Table A.2. Integrated CH$_3$OH line intensities in units of Jy beam^{-1} km s^{-1} towards B35A$-$5.

Source	5_0-4_0 E$^+$	5_1-4_1 E$^-$	5_0-4_0 A$^+$	5_1-4_1 E$^+$	5_2-4_2 E$^-$
B35A$-$5	0.27 ± 0.10	0.77 ± 0.18	1.03 ± 0.22	0.29 ± 0.11	0.20 ± 0.09
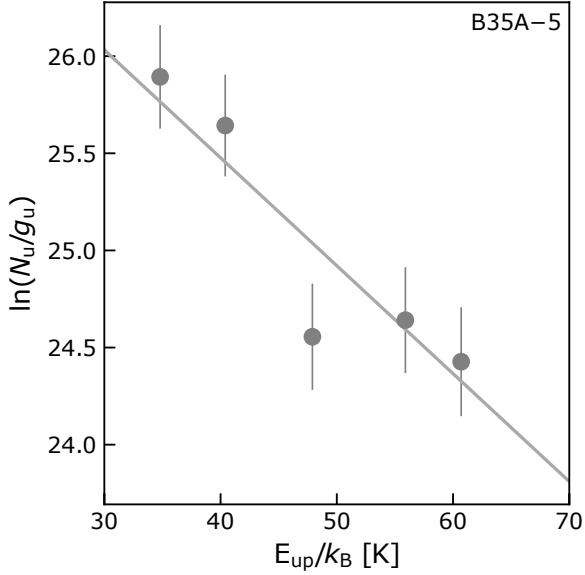
Fig. A.2. Rotational diagram of CH$_3$OH for B35A$-$5. The solid line displays the fixed slope for $T_{\rm rot} = 25$ K. Error bars are for 1σ uncertainties. The derived column density is shown in Table 3.

been taken from the Cologne Database for Molecular Spectroscopy (CDMS; Müller et al. 2001), Jet Propulsion Laboratory (JPL; Pickett et al. 1998), and Leiden Atomic and Molecular Database (LAMDA; Schöier et al. 2005) spectral databases. The adopted formalism assumes LTE conditions and, more

specifically, optically thin line emission, homogeneous source filling the telescope beam, and level populations that can be described by a single excitation temperature. According to the treatment by Goldsmith & Langer (1999) and under the aforementioned conditions, the integrated main-beam temperature $\int T_{\rm MB}\, dv$ and the column density N_u in the upper energy level u are related by:

$$N_u = \frac{8\,\pi\,k_B\,\nu^2}{h\,c^3\,A_{\rm ul}} \int T_{\rm MB}\, dv, \tag{A.2}$$

where k_B is the Boltzmann constant, ν is the transition frequency, h is the Planck constant, c is the speed of light, and $A_{\rm ul}$ is the spontaneous Einstein coefficient of the transition. The total column density $N_{\rm tot}$ and the rotational temperature $T_{\rm rot}$ are related to the column density N_u in the upper energy level u (Goldsmith & Langer 1999) by:

$$\frac{N_u}{g_u} = \frac{N_{\rm tot}}{Q(T_{\rm rot})} e^{-E_u/k_B T_{\rm rot}}, \tag{A.3}$$

where g_u is the upper level degeneracy, $Q(T_{\rm rot})$ is the rotational partition function, k_B is the Boltzmann constant, and E_u is the energy of the upper level u. In summary, the column densities were calculated using the formalism of Goldsmith & Langer (1999) but assuming a fixed rotational temperature equal to 25 K (Craigon 2015; Reipurth & Friberg 2021). Figure A.2 displays the rotational diagram of CH$_3$OH for B35A$-$5. Only CH$_3$OH transitions above 5σ were considered. The uncertainties on the gas column densities were estimated based on the rms noise of the spectra and on the $\sim$20% calibration uncertainty.
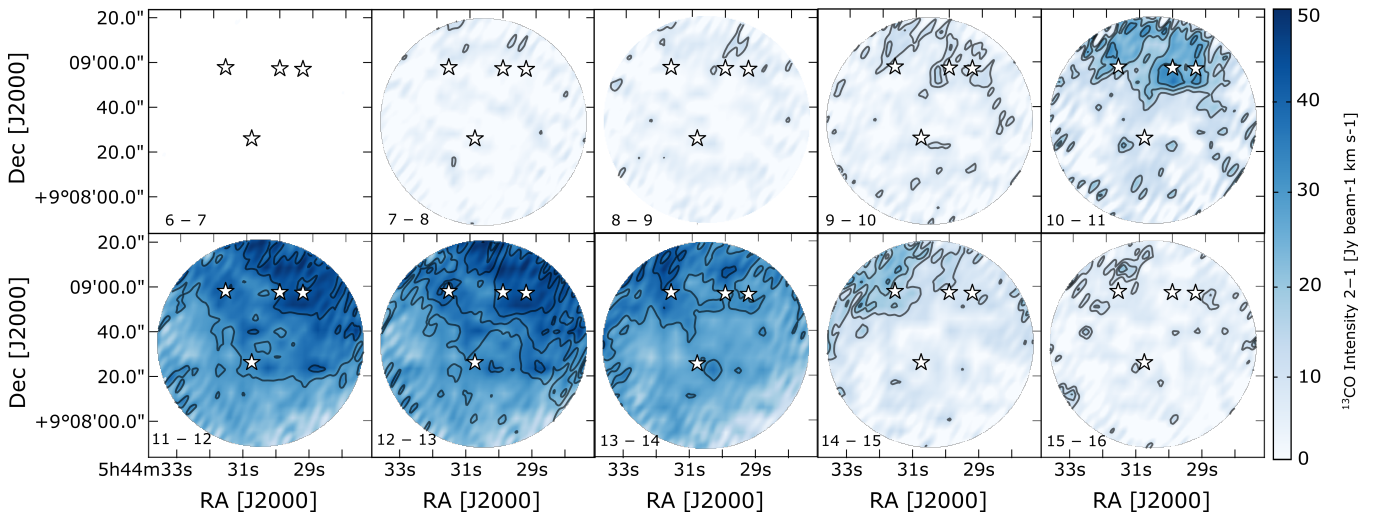
Fig. A.3. Channel maps for ^{13}CO $J = 2-1$ with velocity range 6–16 km s^{-1} in channels of 1 km s^{-1}. Contours start at 5σ and follow in steps of 5σ.
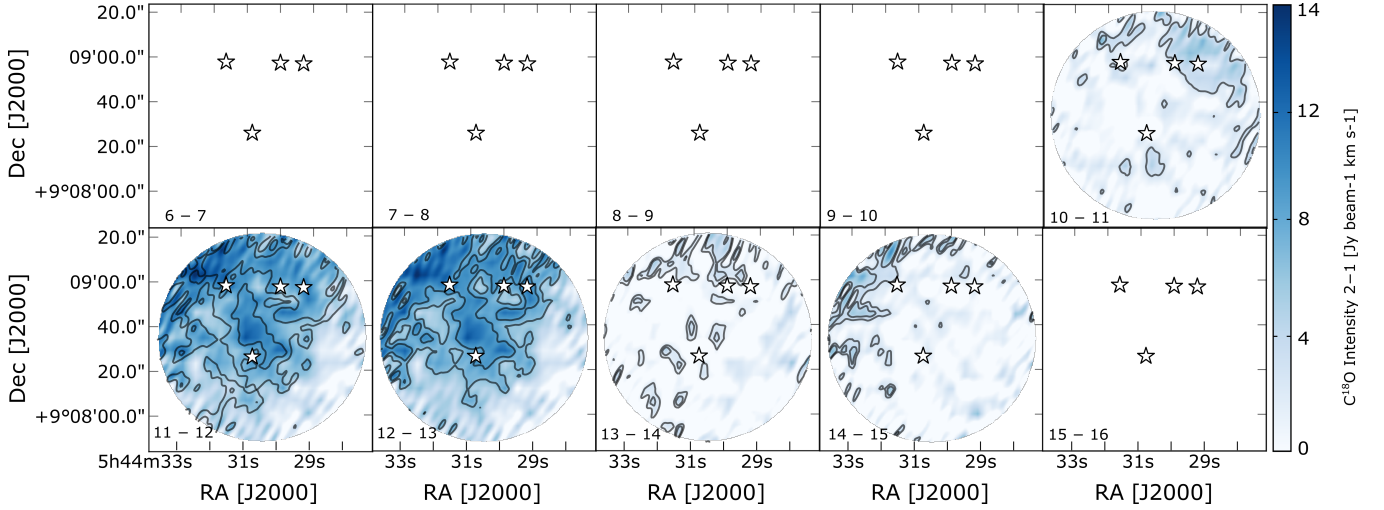
Fig. A.4. Channel maps for C^{18}O $J = 2$−1 with velocity range 6–16 km s^{-1} in channels of 1 km s^{-1}. Contours start at 5σ and follow in steps of 5σ.
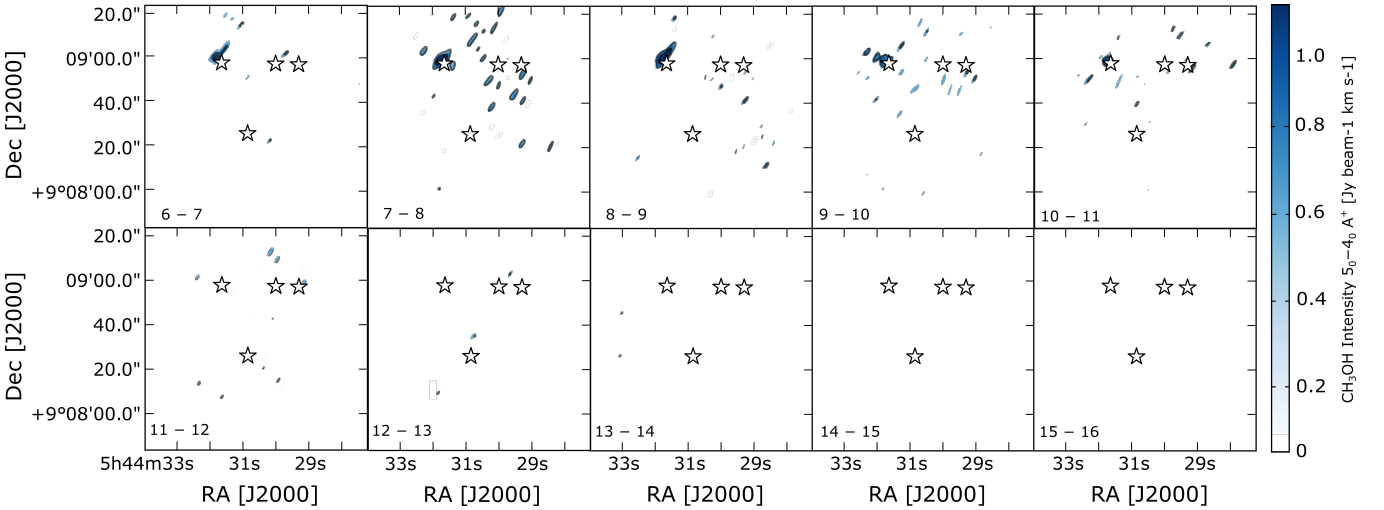
Fig. A.5. Channel maps for CH$_3$OH $J = 5_0$−4_0 A$^+$ with velocity range 6–16 km s^{-1} in channels of 1 km s^{-1}. Contours start at 5σ and follow in steps of 5σ.

Appendix B: H$_2$ column density from visual extinction

Table B.1. Photometry of B35A−3.

Object	1.235 μm [a] [mJy]	1.662 μm [a] [mJy]	2.159 μm [a] [mJy]	3.6 μm [b] [mJy]	4.5 μm [b] [mJy]	5.8 μm [b] [mJy]	8.0 μm [b] [mJy]
B35A−3	0.067	0.442 ± 0.0871	7.31 ± 0.229	44.59 ± 2.6	101 ± 6.9	156 ± 8.09	205 ± 9.97

**Notes.** [a] From 2MASS (Skrutskie et al. 2006). [b] From IRAC (Evans et al. 2014).

The production of the H$_2$ column density map was accomplished by using the visual extinction (A_V) values for B35A tabulated in the c2d catalogue[6]. No A_V values are reported for B35A−2 or B35A−3 in the catalogue. As a result, the visual extinction for B35A−3 was retrieved by de-reddening its SED at the J, H, and K 2MASS photometric points of Table B.1 to fit a first blackbody and then fit a second blackbody to model the infrared excess at

the IRAC photometric points (see Fig. B.1). The extinction in the H band (A_H) was then calculated using the equation (Chapman et al. 2009):

$$A_\lambda = -2.5 \log \left[\left(\frac{F_\lambda}{B_\lambda} \right) \left(\frac{1}{k} \right) \right], \tag{B.1}$$

where λ is the wavelength corresponding in this case to the H band (1.662 μm), F$_\lambda$ is the observed flux at the selected λ, k is a scaling factor, and B$_\lambda$ is the blackbody function. The extinction

---

[6] https://irsa.ipac.caltech.edu/data/SPITZER/C2D/cores.html
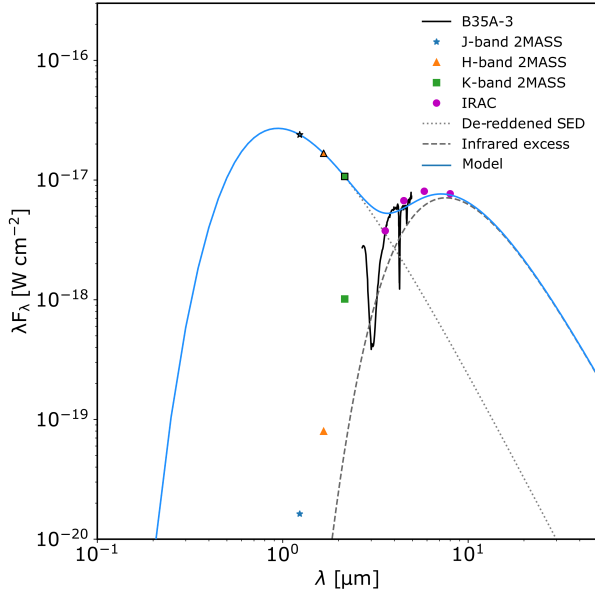
Fig. B.1. SED of B35A−3, which was modelled to determine its visual extinction. The dotted and dashed lines represent the blackbody functions used to model the stellar component and the infrared excess, respectively. The solid line is the sum of the two contributions.

in the H band was then converted to visual extinction using the equation:

$$A_V = 5.55 A_H \text{(mag)}, \qquad (B.2)$$

where the conversion factor is taken from Weingartner & Draine (2001). The adopted extinction law takes into account the dust model from Weingartner & Draine (2001) for $R_V = 5.5$ designed for the dense ISM and used by the c2d collaboration (Chapman et al. 2009; Evans et al. 2009). No NIR photometry data are available for B35A−2, and thus the A_V for this source was obtained by interpolating all the tabulated visual extinction values for B35A taken from the c2d catalogue, including the A_V value for B35A−3. The obtained visual extinction map of B35A was then converted to an H_2 column density map using the relation established for dense ISM gas (Evans et al. 2009):

$$N_{H_2} = 1.37 \times 10^{21} \text{cm}^{-2} (A_V/\text{mag}). \qquad (B.3)$$